Bacterial H-NS contacts DNA at the same irregularly spaced sites in both bridged and hemi-sequestered linear filaments

Beth A. Shen[1], Christine M. Hustmyer[1], Daniel Roston[1,2], Michael B. Wolfe[1], and Robert Landick[1,3]

[1]Department of Biochemistry, University of Wisconsin–Madison, Madison, WI 53706
[2]Current address: Department of Chemistry and Biochemistry, University of California San Diego, La Jolla, CA 92093
[3]Department of Bacteriology, University of Wisconsin–Madison, Madison, WI 53706

*To whom correspondence should be addressed: rlandick@wisc.edu

Highlights:

- Tethered-nuclease mapping (TEN-map) of H-NS DNA-binding domains detects DNA contacts
- Bridged and linear H-NS filaments use the same DNA contact sites
- H-NS–DNA contacts are unevenly spaced with ~10 bp average separation
- AT-steps, minor groove width, and electrostatic potential best predict contact sites

Keywords:

bacterial chromatin; H-NS; FeBABE; MD simulation; nucleoprotein; gene regulation

Select Abbreviations:

DBD, DNA binding domain; DBP, DNA binding protein; FeBABE, Fe(III) (S)-1-(p-Bromoacetamidobenzyl)ethylenediaminetetraacetate; Fe^{2+}·EDTA–H-NS, H-NS derivatized with an Fe^{2+}·EDTA nuclease; MD, molecular dynamics; NTD, N-terminal domain; ·OH, hydroxyl radical; RNAP, RNA polymerase

SUMMARY

Gene silencing in bacteria is mediated by chromatin proteins, of which *Escherichia coli* H-NS is a paradigmatic example. H-NS forms nucleoprotein filaments with either one or two DNA duplexes. However, the structures, arrangements of DNA-binding domains (DBDs), and positions of DBD–DNA contacts in linear and bridged filaments are uncertain. To characterize the contacts that silence transcription by RNA polymerase, we combined ·OH footprinting, molecular dynamics, statistical modeling, and DBD mapping using a chemical nuclease (Fe^{2+}-EDTA) tethered to the DBDs (TEN-map). We find that H-NS DBDs contact DNA at indistinguishable locations in bridged or linear filaments and that the DBDs vary in orientation and position with ~10-bp average spacing. Our results support a hemi-sequestration model of linear-to-bridged H-NS switching in which linear filaments able to inhibit only transcription initiation switch to bridged filaments able to inhibit both initiation and elongation using the same irregularly spaced DNA contact sites.

42 **INTRODUCTION**

43 Extensive study of nucleosome-based chromatin structure has provided broad insight into
44 mechanisms of chromatin-mediated gene regulation in eukaryotes (Cook and Marenduzzo, 2018;
45 Luger et al., 1997; Talbert et al., 2019). For bacteria, however, an analogous understanding of
46 chromosomal gene regulation remains elusive in part due to the diverse and complex DNA-
47 binding properties of the multiple DNA-binding proteins (DBPs) that generate bacterial
48 chromatin (Dame et al., 2020; Grainger, 2016; Shen and Landick, 2019). The γ-proteobacterial
49 histone-like nucleoid structuring protein (H-NS; 15 kDa monomer) provides a paradigmatic
50 model for this complexity (Grainger, 2016; Qin et al., 2019). H-NS, which contains two
51 oligomerization sites in its N-terminal domain (NTD) and a C-terminal DNA binding domain
52 (DBD), forms gene-silencing, oligomeric filaments on ~15% of the *E. coli* genome by targeting
53 AT-rich DNA, notably on pathogenicity operons (e.g. SPI-1 in *Salmonella*), surface-antigen
54 operons (e.g. LPS biosynthesis in *Escherichia coli*), and horizontally acquired genes (e.g. *bgl*
55 operon in *E. coli*) (Figure 1A,B) (Gawade et al., 2020; Grainger et al., 2006; Kahramanoglou et
56 al., 2011; Lucchini et al., 2006; Navarre et al., 2006; Sankar et al., 2009).

57 H-NS dimers oligomerize on DNA through head–head and tail–tail NTD contacts into
58 filaments that adopt either linear or bridged conformations in which H-NS interacts with one or
59 two segments of duplex DNA, respectively (Figure 1A,B) (Arold et al., 2010; Dame et al., 2006;
60 Dame et al., 2000; Gordon et al., 2011; Kotlajich et al., 2015; Liu et al., 2010; Ulissi et al.,
61 2014). The DBD forms an AT-hook-like structure that binds the narrow minor groove of AT-rich
62 DNA (Gordon et al., 2011), consistent with H-NS filament formation on ~15% of the *E. coli*
63 genome with above-average AT content that may reflect acquisition via horizontal gene transfer
64 (Grainger et al., 2006). A flexible linker connecting the DBD and NTD enables DBD–DNA
65 contacts (Gao et al., 2017; Gulvady et al., 2018). However, in some conditions, a subset of DBDs
66 is proposed to interact with the NTD rather than DNA yielding a hemi-sequestered, linear
67 conformation of H-NS–DNA filaments (Shahul Hameed et al., 2018; van der Valk et al., 2017)
68 (Figure 1A).

69 Bridged or linear H-NS filaments may inhibit transcription initiation by RNA polymerase
70 (RNAP) by occluding promoters (Srinivasan et al., 2013) and bridged filaments may trap RNAP
71 at promoters (Dame et al., 2002; Shin et al., 2005). However, only bridged but not linear
72 filaments inhibit transcript elongation by RNAP, which is proposed to occur via a topological
73 trapping mechanism (Figures 1A and S1) (Boudreau et al., 2018; Kotlajich et al., 2015).
74 Switching between linear and bridged states, DNA avidity, and thus H-NS effects on gene
75 expression may be modulated in vivo by changes in H-NS levels, H-NS filament modifiers like
76 Hha, cellular solutes and thus environmental conditions, and temperature (Boudreau et al., 2018;
77 Kotlajich et al., 2015; Qin et al., 2020; van der Valk et al., 2017; Zhao et al., 2021a; Zhao et al.,
78 2021b).

79 It remains unclear how the DBDs are arranged on DNA within either linear or bridged H-
80 NS filaments and if the contacts change in the switch between linear and bridged conformations
81 that differentially affect steps in transcription. DNase and ·OH footprinting experiments reveal
82 nucleation at AT-rich high-affinity sites and H-NS oligomerization with an apparent periodicity
83 of DBD contacts every ~10 bp (Bouffartigues et al., 2007; Ulissi et al., 2014; Will et al., 2015).
84 Additionally, single-molecule pulling experiments show that strong DBD–DNA contacts at ~10-
85 or ~20-bp intervals are common in bridged filaments (Dame et al., 2006). A prevalent model for
86 H-NS filament organization based on an NTD crystal structure predicts ~30-bp spacing of DBDs
87 in a bridged filament (Arold et al., 2010). Although H-NS is known to bind AT-rich DNA
88 (Gordon et al., 2011) the locations of the H-NS DBDs in filaments relative to DNA sequence
89 features is not well defined. Because a flexible linker connects the DBDs to the filament-forming
90 NTD, the extent to which DBD–DNA contacts within a filament are regularly spaced is also
91 unclear. New approaches are needed to determine how DNA sequence governs DBD location
92 and the arrangement of DBDs in an H-NS filament.

93 To gain insight into the organization of DBD locations in filaments, we developed and
94 applied a multimodal approach that combines a novel DBD-mapping method using a tethered
95 chemical nuclease (TEN-map), hydroxyl radical (·OH) footprinting, computational molecular
96 dynamic (MD) simulations, and rigorous statistical analysis and modeling. Our results reveal that

97 DBDs contact DNA irregularly in an H-NS filament but at the same locations in bridged and
98 linear filaments. They also confirm the hemi-sequestration model of linear-to-bridged H-NS
99 switching and providing a conceptual framework for understanding the mechanism of gene
100 silencing by H-NS and related proteins in bacteria.

101 **RESULTS**

102 **Tethered-nuclease mapping (TEN-map) reveals H-NS DBD locations in H-NS filaments**
103 To determine the spacing and orientation of DBDs within an H-NS filament, we sought a method
104 that could reveal DBD location and orientation on DNA as a complement to conventional ·OH
105 footprinting, which defines regions of protection on DNA but not which part of a protein is
106 responsible for the protection. To that end, we attached the chemical nuclease Fe^{2+}·EDTA to the
107 H-NS DBD to enable tethered nuclease mapping of DBD contacts on DNA (TEN-map; Figure
108 1C,D). TEN-map reveals the locations and orientations of DBDs by generating hydroxyl radicals
109 (·OH) that can cleave the nearby DNA backbone within ~10 Å from the Fe moiety (Cheal et al.,
110 2009; Greiner et al., 1997; Rana and Meares, 1991). For example, this method detects DNA
111 contacts by the *E. coli* RNAP α subunit CTDs that also bind the minor groove of promoter DNA
112 and are tethered by flexible linkers (Murakami et al., 1997).

113 For TEN-map, Fe^{2+}·EDTA was attached to Cys substituted for E102 in the H-NS DBD by
114 reaction with FeBABE (Fe(III) (*S*)-1-(*p*-bromoacetamidobenzyl)ethylenediaminetetraacetate)
115 (Greiner et al., 1997; Rana and Meares, 1991). We chose E102 because it is near DNA but not
116 part of the DBD–DNA interface in a model of the H-NS DBD (Gordon et al., 2011), is predicted
117 to remain solvent exposed in H-NS filaments, and can be replaced by Ala without effect on H-
118 NS DBD binding to DNA (Gordon et al., 2011) (Figure 1C). Modeling of Fe^{2+}·EDTA attached
119 to C102 DBD predicted that the chelated Fe^{2+} remains near the DNA but would not interfere
120 with the H-NS–DNA interface (Figure 1C; see below). *E. coli* H-NS naturally contains Cys at
121 position 21 in the NTD site 1 (Figure 1B). Therefore, we constructed, overexpressed, and
122 purified recombinant H-NS C21S E102C. Conjugation with FeBABE yielded the tethered
123 nuclease H-NS (Fe^{2+}·EDTA–H-NS).

124 We first tested whether Fe^{2+}·EDTA–H-NS could form H-NS filaments and inhibit transcript
125 elongation by RNAP as observed previously for wild-type H-NS (Boudreau et al., 2018;
126 Kotlajich et al., 2015). We used a 1.5 kb duplex DNA in which the upstream and downstream
127 regulatory elements (URE and DRE) from the H-NS silenced *bgl* operon (Dole et al., 2004;
128 Nagarajavel et al., 2007) were transcribed from a strong λP_R promoter positioned to mimic

129 natural transcription of the *bglF* antisense promoter (Figures 1A and 1E). Unconjugated C21S
130 E102C H-NS at ~66 H-NS/kb DNA, conditions found previously to favor bridged filaments,
131 stimulated pausing by RNAP whereas linear filaments formed at ≥200 H-NS/kb had much less
132 effect (Figure 1E; compare to WT H-NS in Figure S1). Both C21S H-NS and C21S, E102C H-
133 NS treated with FeBABE stimulated pausing similarly to wild-type bridged H-NS filaments but
134 required higher concentrations to show effects (Figure 1F). However, even the highest levels of
135 the FeBABE-treated H-NS achievable in this assay (250 H-NS/kb) still inhibited elongation. We
136 concluded that bridged Fe^{2+}·EDTA–H-NS filaments stimulate pausing similarly to wild-type H-
137 NS but that the conjugated H-NS either was constitutively bridged or was partially inactivated by
138 the conjugation reaction so that concentrations of active H-NS needed to form linear filaments
139 could not be achieved. Shahul Hameed et al. (2018) report E102 may interact with the H-NS
140 NTD in linear filaments, which could explain constitutive bridging by Fe^{2+}·EDTA–H-NS.

141 To probe the structure of nucleoprotein filaments formed by Fe^{2+}·EDTA–H-NS, we
142 visualized them using an electrophoretic mobility shift assay (EMSA) (Figure S2). Wild-type
143 and C21S H-NS formed the slower and faster migrating bands at 100 and 250 H-NS/kb DNA,
144 characteristic of bridged and linear filaments, respectively (Boudreau et al., 2018; Kotlajich et
145 al., 2015). However, neither C21S E102C H-NS nor Fe^{2+}·EDTA-conjugated H-NS appeared able
146 to form linear filaments; both exhibited shifts to more slowly migrating filaments at 250 H-
147 NS/kb rather than to faster migrating linear filaments. Both C21S and C21S–E102C H-NS
148 treated with FeBABE required higher concentrations to form filaments, which may reflect partial
149 loss H-NS activity during biochemical manipulation. These results confirm that Fe^{2+}·EDTA–H-
150 NS forms bridged H-NS filaments but suggest that these filaments are constitutively bridged.
151 Since even unconjugated C21S–E102C H-NS was unable to form linear filaments, our results are
152 consistent with the idea that E102 contributes to hemi-sequestration of the DBD via interactions
153 with the NTD in linear H-NS–DNA nucleoprotein filaments (Shahul Hameed et al., 2018).

154 To probe the locations of the bridged H-NS DBDs on DNA with TEN-map, we chose a 146-
155 bp fragment of the *bgl* operon encompassing the DRE that is known to bind H-NS well in vitro
156 (Figures 1A and S3) (Dole et al., 2004; Nagarajavel et al., 2007). The 146-bp DRE fragment

157 could accommodate 10–15 H-NS DBDs (assuming a binding-site size of 10–15 bp) and enabled
158 single-nt resolution of cleavage when analyzed by denaturing PAGE (Figure 2). We probed
159 TEN-map cleavage on both strands of the 146-bp DRE fragment separately by positioning a
160 5′-^{32}P label at one end of the top or bottom DNA strands. After formation of filaments,
161 phosphodiester backbone cleavage *via* hydrogen abstraction from DNA sugars was triggered by
162 addition of H_2O_2 and ascorbic acid to generate ·OH by the Fenton reaction (Balasubramanian et
163 al., 1998). We observed robust cleavage patterns for both DNA strands at Fe^{2+}·EDTA-H-NS
164 ≥1 μM, confirming specific positioning of the DBDs bound to the DRE fragment (Figure 2A,B).
165 To quantify the cleavage patterns, we calculated peak areas for cleavage signals at each bp by
166 densitometric analysis (Das et al., 2005). Cleavage maxima were spaced at irregular intervals on
167 both strands and remained unchanged in location up to 5 μM Fe^{2+}·EDTA–H-NS (Figure 2C,D).

168 To confirm the TEN-map cleavages resulted from Fe^{2+}·EDTA tethered to H-NS, we verified
169 that the TEN-map pattern was distinct from ·OH cleavage of free DNA or DNA bound by H-NS
170 when Fe^{2+}·EDTA was free in solution rather than tethered (Figure S4). ·OH cleavage using
171 untethered Fe^{2+}·EDTA corresponds to conventional ·OH footprint of H-NS and resembled but
172 was not identical to the TEN-map pattern. The resemblance is expected because the bound H-NS
173 DBD excludes ·OH from DBD–DNA interfaces regardless of the source of ·OH; the differences
174 in two patterns confirmed that TEN-map gives information about DBD positioning on DNA
175 based on Fe^{2+}·EDTA tethering to one side of the DBD bound in a DNA minor groove; Figure
176 1C).

177 Because the DRE fragment used for TEN-map was a short, linear DNA, we asked if either
178 the DNA ends or the DNA fragment length might influence phasing of DBDs along the DNA.
179 We first compared TEN-map cleavage of the 146-bp DRE fragment to that of a 151-bp fragment
180 identical to the 146-bp fragment except for 5 bp added to the ^{32}P-labeled end (Figure S5A). We
181 observed identical cleavage patterns for these two fragments, establishing that the DBD locations
182 were determined by the underlying DNA sequence rather than being phased from a nearby DNA
183 end (Figure S5B). We next compared TEN-map of the 146-bp DRE fragment to that of a 549-bp
184 fragment with the same ^{32}P-labeled end (top strand) but extended 403 bp in the direction

185 opposite the ^{32}P-labeled end (Figure S5C). The TEN-map patterns were essentially identical for
186 these DNAs (Figure S5D), except for a stronger peak at position ~112 on the long DRE DNA
187 fragment. Cleavage at this position may be stronger on the 549-bp DNA because the H-NS
188 filament is stabilized at the position by the adjacent DNA absent on the 146-bp DNA. We
189 conclude that H-NS–DBD contacts are determined by the underlying DNA sequence and not
190 binding of H-NS to flanking regions or to a DNA end.

191 **H-NS DBD locations are unchanged in obligately bridged filaments or by Mg^{2+}**

192 We next sought to verify that the H-NS filaments modified at E102 were always bridged in the
193 TEN-map assay. For this purpose, we first used a previously developed bridging–pulldown assay
194 (van der Valk et al., 2017) to generate unambiguously bridged filaments (Figure 3A and S6). In
195 the bridging–pulldown assay, H-NS–DNA filaments are captured from solution by DNA-coated
196 magnetic beads. Capture requires H-NS bridging between the bead-bound and unbound DNAs.
197 We incubated streptavidin beads pre-loaded with a 685-bp, biotinated bait DNA with a mixture
198 of Fe^{2+}·EDTA-H-NS, unmodified H-NS, and unbiotinated 549-bp DRE-containing fragment 5′
199 ^{32}P–end labeled on the top strand (Figure 3A). Bridged filaments, whose formation was
200 unaffected by the presence of conjugated H-NS, were magnetically separated from unattached
201 filaments and TEN-map cleavage was activated (Figure S6A). These obligately bridged cleavage
202 patterns were indistinguishable from those observed without bead-based capture (Figure 3A and
203 S7), confirming that the TEN-map assay reports the locations of bridged H-NS DBDs. As an
204 additional test, we asked how elevated Mg^{2+}, which stimulates bridging at concentrations >5 mM
205 (Liu et al., 2010), would affect the TEN-map assigned DBD locations. We found that DBD
206 locations were unaffected by elevated Mg^{2+} (8 mM vs. ~0.3 μM) at either high or low
207 H-NS/DNA ratios (Figures 3B and S8). In agreement with the EMSA assay (Figure S2), these
208 results indicate that H-NS filaments with Fe^{2+}·EDTA attached to C102 in the DBD are
209 constitutively bridged.

210 **Wild-type H-NS DBD ·OH footprints on DNA are unchanged during bridged-to-linear**
211 **switching**
212 Although the TEN-map cleavage pattern revealed H-NS binding positions within a bridged
213 filament, it could not probe whether the DBDs change locations in the switch from bridged to
214 linear because the derivatized H-NS was constitutively bridged. However, this switch can be
215 probed simply by increasing the concentration of H-NS from ~66 H-NS/kb DNA (bridged
216 filaments) to ≥200 H-NS/kb DNA (linear filaments) (Kotlajich et al., 2015) (Figure 4A). Since
217 the DBDs confer patterns of protection of DNA in conventional ·OH footprinting experiments,
218 we reasoned that assaying ·OH footprints as a function of H-NS concentration should reveal any
219 changes in DBD locations that occur in the switch from bridged to linear filaments. Therefore,
220 we generated ·OH footprints of wild-type H-NS on the DRE encompassing the appropriate
221 ranges of H-NS concentrations (Figures 4 and S9). We normalized ·OH cleavage as a function of
222 H-NS concentration to the unprotected cleavage pattern to correct for intrinsic DNA reactivity
223 (Burkhoff and Tullis, 1988). Strikingly, the H-NS footprint positions did not change as H-NS
224 concentration was increased from a range that favors bridging to well above the concentration
225 that switches filaments to the linear conformation (Figure 4B,C).

226 As a further test of the conclusion that DBD contacts remain the same in bridged and linear
227 H-NS filaments, we examined previously reported H-NS footprints on different DNA sequences
228 for which H-NS/DNA ratios were reported. Four studies met these criteria (Lucht et al., 1994;
229 Moreira et al., 2011; Ulissi et al., 2014; Will et al., 2018). Despite the use of different
230 footprinting methods (DNaseI or ·OH) and different DNA sequences, no change in apparent
231 DNA contacts at different DNA concentrations encompassing both bridged and linear conditions
232 was evident in any of these studies (Table S1). These prior results thus strongly support our
233 conclusion that bridged and linear H-NS–DNA filaments use the same DNA contact sites with
234 unchanged spacing in the switch from bridged to linear conformations.

235 **MD simulation and statistical modeling reveal H-NS DBD spacing and orientation**
236 Although both TEN-map and ·OH footprinting indicate unchanged DNA contact sites and
237 spacing in bridged and linear filaments, neither the precise placement nor the orientation of the

238 H-NS DBDs are immediately apparent from the cleavage patterns. Thus, to assign locations and
239 orientations of the DBDs from our TEN-map and ·OH footprinting data, we used a combination
240 of molecular dynamic and statistical modeling. We first generated predicted cleavage and
241 protection patterns for a bound DBD in TEN-map and ·OH footprinting by molecular modeling.
242 For the TEN-map predictions, we modified a structural model of an H-NS DBD bound to the
243 minor groove of DNA (Gordon et al., 2011) to include Fe^{2+}·EDTA tethered to the E102C
244 substitution and used it to seed an MD simulation of ·OH generation (Figure 5A). The
245 simulations generated a probability distribution of distances between all possible conformations
246 of the tethered Fe^{2+} and each nucleotide in the duplex DNA strands to which the DBD is bound
247 (arbitrarily designated strands A and B in the model). We assumed that the cleavage propensity
248 at each nucleotide in the DNA fragment is directly proportional to the local concentration of ·OH
249 at that nucleotide, which we estimated by a diffusion model for ·OH centered at the Fe^{2+}.
250 Because some nucleotides are shielded from the solvent by the bound DBD, we scaled the
251 concentration of radicals according to the solvent-accessible surface area of the putative cleavage
252 site (Figure 5B) (Balasubramanian et al., 1998). Modeling based on these assumptions yielded an
253 estimate of the relative cleavage propensity at each nucleotide in the duplex DNA bound by the
254 DBD (Figure 5A; see Methods).

255 When the predicted pattern of ·OH cleavage was displayed on B-form DNA, foci of
256 cleavage were evident on each DNA strand offset from the location of the DBD in the minor
257 groove (Figure 5C). The maximum peak of cleavage was predicted to occur at nucleotide +10 of
258 strand A and was flanked by two smaller predicted cleavage peaks in strand B. Adjacent to these
259 sites of high predicted cleavage were sites of protection from cleavage, which resulted from
260 shielding of DNA by the bound DBD. We note that this model does not account for possible
261 contributions to DNA cleavage by ·OH generated from any Fe^{2+}·EDTA-DBDs not bound to
262 DNA. These contributions are assumed to be non-specific, to contribute to background DNA
263 cleavage, and thus to be captured in the model by solvent shielding by the bound DBD. In other
264 words, bound DBDs are expected to generate local cleavage patterns that reflect localization of
265 Fe^{2+}·EDTA near DNA whereas unbound DBDs are assumed to generate background cleavage
266 from unlocalized ·OH.

267 We applied a similar analysis to the untethered ·OH footprinting data by using only the
268 calculated solvent exclusion from DNA by the bound DBD to predict protection patterns (Figure
269 5B). These predicted protection patterns were not completely symmetric due to asymmetric DBD
270 shape when bound to the DNA minor groove in the model (Figure 5D). Thus, although much less
271 robust than for TEN-map, the predicted protection patterns could be compared to ·OH footprints
272 for DBDs bound in either orientation on the DRE fragment.

273 To generate robust TEN-map and ·OH footprint signals to compare to the predictions, we
274 first used Bayesian linear regression of the DNA cleavage signals as a function of H-NS
275 concentration to assign a single signal strength for each DNA nucleotide on each strand (Figure
276 S10). This analysis was possible because only the intensities and not the locations of the TEN-
277 map cleavages changed as a function H-NS concentration. For the TEN-map data, we centered
278 the normalized cleavage signals for each H-NS concentration at zero (Figure S10A,D), and then
279 fit a Bayesian linear regression model to the signal at each position (Figure S10B). We then used
280 the slopes of these linear-regression fits to generate single-value traces of TEN-map cleavage on
281 each DNA strand for which robust cleavage had a large, positive value (Figures S10C and
282 S10E). Visualization of the H-NS-dependent cleavage on B-form DNA revealed a pattern of
283 cleavage maxima and minima consistent with potential DBD locations (Figure 5E). We used a
284 similar procedure to generate single-value traces of ·OH footprint data on each DNA strand
285 (Figures 5F and S11), for which robust protection had a large, negative value (Figures S11C and
286 S11E).

287 These single-value traces for both the TEN-map and ·OH footprint results were then
288 compared to the predicted patterns for the respective methods, scanning each nucleotide position
289 on each DRE DNA strand (Figure 5G,H). We calculated Manhattan distances between these
290 predicted cleavage patterns for the DBDs and the observed cleavage traces generated by the
291 linear regression models (Figures S12). The Manhattan distance is the sum of absolute
292 differences between of sets of points; a lower score indicates a closer match (see Methods). The
293 TEN-map and ·OH footprinting match scores revealed similar patterns of DBD interactions with
294 the DRE DNA (Figure S12A and B). To estimate the statistical significance of the match scores,

295 we compared them to values obtained from a Monte Carlo permutation test (see Methods). The
296 match scores could then be converted to *p*-value estimates of the probability they could arise by
297 chance (Figure S12C and D).

298 To generate a final model of the H-NS filament on the DRE DNA, we combined the *p*-
299 values for the TEN-map and ·OH footprint methods into a single prediction of DBD locations
300 (Figure 6A and S12E). This integrated probability calculation predicted seven DBD locations in
301 the reverse orientation with $p \leq 0.05$ and variable spacing of 8-17 bp between the center of the
302 DBD contacts (45R, 62R, 71R, 81R, 93R, 106R, and 114R; 106R was included because its *p*-
303 value was essentially indistinguishable from 0.05). These seven could represent contacts made
304 by a single bridged or linear H-NS–DNA filament (Figure 6B). Three weaker potential DBD
305 contacts in the forward orientation also were predicted (50F, 66F, 88F). The forward-oriented
306 DBDs were offset by ~5 bp from nearby stronger predictions for DBDs in the reverse
307 orientation. This offset prevents steric clash with the more robustly predicted reverse DBDs if
308 the forward DBDs are placed on the DRE DNA (Figure 6B). It is thus unclear whether they
309 might represent alternative contacts of the same DBD or weak contacts by an adjacent DBD.

310 This model of H-NS DBD interactions with the DRE DNA supports the following
311 conclusions. First, DBD locations within the H-NS filament are irregularly spaced along the
312 DNA duplex, with separations varying from 8-17 bp. Second, these spacings are broadly
313 consistent with DBD contacts approximately every 10 bp along DNA possibly skipping one
314 contact between 45 and 62, consistent with previous analyses of H-NS–DNA interactions. Third,
315 we cannot exclude the possibility that DBDs might alternate between adjacent contact sites in the
316 forward and reverse orientations. Finally and most importantly, the DBDs in both bridged and
317 linear H-NS filaments do not contact DNA with rigidly fixed spacing but rather assume positions
318 within a window of possible locations likely based on the highest affinity to local DNA sequence
319 features (see Discussion).

320 **TA steps, minor groove width, and electrostatic potential best predict DBD locations**

321 Having identified the binding locations of the H-NS DBDs on the DRE fragment, we next asked
322 which features of the DRE DNA best predicted these locations. A prior analysis of sequences

323 most tightly bound by the DBD of the close H-NS paralog Lsr found variable preference for AT-
324 rich 4mer sequences (AAAA, AAAT, AATT, ATTT, TTTT, ATAA, ATAT, ATTA, AATA,
325 TAAA, TAAT, TATA, TATT, TTAA, TTAT, or TTTA) with TA-step-containing 4mers having
326 highest affinity when the 4mers are located in regions of high A/T content (Gordon et al., 2011).
327 Overall AT-richness, A-tracts, or a specific high-affinity sequence (Lang motif) also have been
328 postulated to explain H-NS–DNA binding specificity (Gordon et al., 2011; Lang et al., 2007;
329 Navarre et al., 2006). In addition to sequence patterns, it also is possible to predict DNA
330 structural features like minor groove width (MGW) and electrostatic potential in the minor
331 groove (EP) (Chiu et al., 2017; Chiu et al., 2016; Zhou et al., 2013), and MGW, in particular, is
332 suggested to favor DBD binding (Gordon et al., 2011). We first assessed the presence of these
333 various sequence and structural features in the DRE fragment (Figure 7A). Three features, TA-
334 step, narrow MGW, and low EP were notably enriched at sites bound by the H-NS DBD.

335 To ask if these features were predictive of the H-NS DBD binding sites, we used a LASSO
336 logistic regression model, which calculates the minimum number of variables required to predict
337 an objective function, to assess the predictive contributions of sequence, structural, and
338 electrostatic variables to the DBD binding pattern. We found that our high-confidence DRE
339 DBD locations could be described using only TA-steps, a narrow MGW, and negative
340 electrostatic potential (Figure 7B). As further validation that these three features can predict H-
341 NS DBD locations, we used our regression model to predict H-NS DBD locations in the DRE
342 fragment (Figure 7C). Encouragingly, our model was able to robustly predict the DBD binding
343 sites that match our experimentally determined binding sites. We conclude that TA-steps, MGW,
344 and electrostatic potential are the most useful predictors of H-NS DBD location. Since we
345 observe the same DBD locations in both bridged and linear filaments, these features should be
346 applicable in predicting sequence preferences for either form of the H-NS filament.

347
348

349 **DISCUSSION**

350 We report new insights into the structures of bridged and linear filaments formed by the bacterial
351 gene silencer H-NS by combining two approaches not previously applied to H-NS. First, we
352 mapped contacts of the H-NS DBD using a tethered nuclease (TEN-map) that also causes
353 constitutive bridging. Second, we coupled molecular and statistical analyses of TEN-map and
354 ·OH footprinting data to predict DBD locations on a known mediator of gene silencing, the *E.*
355 *coli bgl* operon DRE. These results yielded three principal insights: (*i*) HNS DBD locations do
356 not change in the switch from linear to bridged filaments, supporting a model of DBD hemi-
357 sequestration in linear filaments; (*ii)* the DBDs do not contact DNA with precisely fixed spacing
358 but rather adjust both contact point and possibly orientation along adjacent minor groove
359 positions; and (*iii*) the positions of the DBDs were best explained by the DNA sequence features
360 AT steps, minor-groove width, and charge distribution.

361 These insights do not depend on complete accuracy of our DBD–DRE model (Figure 6B),
362 which cannot be fully assessed without a high-resolution H-NS–DRE structure. Rather, our
363 model provides a plausible way to visualize the key insights as well as the uncertainties. The
364 constancy of irregular DBD spacing in bridged and linear filaments is our key finding. This
365 feature of H-NS–DNA interaction remains valid even if our DBD placements are somewhat
366 inaccurate. The irregularity and constancy of DBD interactions are compelling even though the
367 signal-to-noise in our data is modest. Indeed, the noisy nature of H-NS–DNA interaction data,
368 also evident in other studies, likely reflects a fundamental property of H-NS. For example, TEN-
369 map signals for the H-NS DBDs are markedly more noisy than observed for RNAP α subunit
370 CTDs bound to promoter DNA (Murakami et al., 1997) (compare Figure 2 to Murakami et al.
371 Figure 5B). The H-NS DBD contacts appear to vary in strength and spacing as a function of
372 DNA sequence for a given H-NS–DNA filament. The contacts may also be somewhat fluid.
373 DBDs alternating in orientation, or on and off DNA, could explain why some DBD–DRE
374 contacts appear weak or as "shadow" contacts offset by ~5 bp (Figures 6 and S12). This fluid
375 and irregular character of DBD contacts may help H-NS vary the extent of gene silencing as a
376 function of cellular composition, temperature, and H-NS modulators like Hha (Boudreau et al.,

377 2018; Kotlajich et al., 2015; Qin et al., 2020; van der Valk et al., 2017; Zhao et al., 2021a; Zhao
378 et al., 2021b).

379 **H-NS DBD contacts to DNA do not change in the switch from bridged to linear**
380 **conformations**

381 A key feature of H-NS-based gene regulation is the capacity of H-NS filaments to switch from
382 binding one DNA duplex as a linear filament to binding two DNA duplexes in a bridged
383 conformation. The extent of DNA bridging *in vivo* and whether it varies among genes or
384 conditions remains unknown. However, the fact that H-NS can block transcript elongation only
385 in the bridged conformation where it creates topological traps to elongating RNAP (Boudreau et
386 al., 2018; Kotlajich et al., 2015) and the clear evidence that H-NS modulates transcription
387 elongation *in vivo* by stimulating ρ-dependent termination (Chandraprakash and Seshasayee,
388 2014; Peters et al., 2012; Saxena and Gowrishankar, 2011) provide strong evidence that bridging
389 occurs to some extent *in vivo*. A structural basis for switching of H-NS between linear and
390 bridged filaments remains to be fully elucidated.

391 The Dame and Arold groups have proposed a hemi-sequestration model of H-NS DBD
392 location that can explain linear-to-bridged switching (Shahul Hameed et al., 2018; van der Valk
393 et al., 2017) . In the hemi-sequestration model, one of the two DBDs present at each tail–tail
394 dimerization interface in an H-NS filament binds to DNA and the second DBD is sequestered
395 through interactions with the N-terminal dimerization domain, possibly aided by buckling of the
396 α-helix connecting the two dimerization interfaces. Thus, the hemi-sequestered or closed
397 conformation enables only linear filament formation whereas the open conformation, which is
398 favored by binding of Mg^{2+} or Hha and may be constitutive in StpA (Boudreau et al., 2018; van
399 der Valk et al., 2017), releases the sequestered set of DBDs so they can bridge to a second DNA
400 duplex (Figure 1A; Figure 8).

401 Our results validate the hemi-sequestration model by documenting the absence of changes in the
402 locations of DBDs in bridged and linear filaments (Figures 3, 4, 6, and S12). This constancy of
403 DBD contacts to DNA is evident both in the lack of effect on ·OH footprints when H-NS
404 concentration is varied from levels known to favor bridging (≤100 H-NS/kb DNA) to

405 concentrations far above those known to create linear filaments by saturating all available
406 binding sites (≥200 H-NS/kb DNA; Figure 4) (Kotlajich et al., 2015). Importantly, the ·OH-
407 footprint pattern evident in conditions favoring linear filaments predicts essentially the same
408 DBD locations predicted for constitutively bridged filaments analyzed by TEN-map (Figure
409 S12). This same observation of no change in footprints at different H-NS/DNA ratios or at high
410 versus low Mg^{2+} concentration, both of which modulate linear–bridged preference, is evident in
411 reports from several other groups (Lucht et al., 1994; Moreira et al., 2011; Ulissi et al., 2014;
412 Will et al., 2018) (Table S1). Taken together, these results strongly favor the hemi-sequestration
413 model of H-NS linear-to-bridged filament switching because the model readily explains use of
414 the same DBD contacts in both bridged and linear filaments.

415 **DBD locations within H-NS filaments are set by DNA sequence rather than precise spacing**
416 Our conclusion that H-NS DBD locations are unevenly spaced in H-NS nucleoprotein filaments
417 is also consistent with previously reported ·OH and DNaseI footprints of H-NS on DNA (Lucht
418 et al., 1994; Moreira et al., 2011; Ulissi et al., 2014; Will et al., 2018) (Table S1). These prior
419 results suggest semi-regular spacing of ~10 bp between H-NS protected sites, but also variation
420 in spacing over a 5–30 bp range between some sites. Our conclusion also is consistent with a
421 single-molecule analysis of H-NS–DNA contacts (Dame et al., 2006). When bridged H-NS
422 filaments are pulled apart with ~22 pN force, H-NS contacts are lost in steps of multiples of ~11
423 bp (~1 helical turn of B-form DNA). However, the ~11-bp steps are not uniform in length.
424 Rather, they frequently deviate in apparent DBD–DNA contact positions by ± ~2 bp, consistent
425 with our observation of DBD contacts spaced by 8–13 bp (Figure 6). Further, many ~11-bp
426 steps give little or no detectable force signature, yielding a mean step size closer to two helical
427 repeats. Consistent with our observation of variable strength DBD signals, some single-molecule
428 contacts may be too weak to give a force signature or some DBDs may remain sequestered by
429 interaction with the H-NS NTD (Shahul Hameed et al., 2018; van der Valk et al., 2017).

430 Consistent with this view of variable H-NS DBD contact spacing, we observed a correlation
431 between the apparent DBD contact positions and DNA sequence features (Figure 7). Thus, DNA
432 sequence likely dictates the lowest free energy arrangement of DBDs within the constraints

433 imposed by their flexible tethers to the H-NS NTD oligomer. Specifically, DBDs were located
434 on the DRE fragment at sequence and shape features that confer high-affinity for H-NS (e.g. TA
435 steps, A-tracts leading to narrow minor groove width and negative EP), but were not observed at
436 lower-affinity sites lacking these features (Figure 7). High affinity for TA steps also was
437 observed in SELEX-like experiments using a DBD from an H-NS paralog (Gordon et al., 2011).
438 Thus, the precise position and orientation DBDs on the minor groove is likely dictated by the
439 best complement in shape and charge to the DBD within reach of the linker. Larger spacings of
440 two or more helical repeats in contacts may reflect the absence of strong binding features near a
441 given tail–tail junction in the H-NS NTD oligomer so that one or both DBDs at a given junction
442 preferentially associate with the NTD.

443 What can this flexibility in DBD arrangement tell us about the structure of H-NS filaments?
444 Our results define neither the specific conformation of the H-NS head–head, tail–tail oligomer
445 nor the conformation of the bound DNA. H-NS–bound DNA is likely to deviate from a canonical
446 B-form helix due to its AT-rich sequence and distortion by H-NS contacts. Nonetheless, our
447 findings can guide future efforts to determine H-NS–DNA nucleoprotein filament structures and
448 may aid understanding regulation of transcription by H-NS family proteins in several ways.

449 First, the DBD locations we find are inconsistent with the H-NS NTD oligomer crystal
450 structure in which long NTD α helix separates the tail–tail junctions by ~100 Å (Arold et al.,
451 2010). This distance would separate the junctions to which two DBD linkers connect by ≥30 bp
452 on a B-form DNA duplex. In a bridged filament, only one of two DBDs at the junction would be
453 available per DNA duplex. It is unlikely that H-NS can distort DNA enough to position one
454 DBD per junction every 8-12 bp even though the 11-aa linker (G85–A95) could stretch up to ~35
455 Å. Other conformations of the NTD have been observed in MD simulations (Shahul Hameed et
456 al., 2018; van der Valk et al., 2017). It seems likely that these or other alternative conformations
457 of the NTD must explain the variable but on average ~10.5 bp DBD spacing in H-NS filaments.

458 Second, the irregular but sequence-dependent pattern of DBD–DNA interactions suggests
459 that the structure of the H-NS–DNA filament itself may be irregular. Buckling of the H-NS NTD
460 and variable extents of sequestration of DBDs via NTD interaction could both support an overall

461 irregular structure. By allowing the DBDs to establish stronger DNA interactions with optimal
462 sequences within range of the linker, an irregular nucleoprotein filament may allow H-NS to
463 bind DNA more tightly than would be possible in a completely regular structure.

464 Finally, an irregular H-NS–DNA nucleoprotein filament structure has important
465 implications for efforts to determine a high-resolution structure of the filament. A high-
466 resolution structure is essential to understand H-NS regulatory function. Although cryo-EM can
467 be used to solve structures of filaments with helically repeating structures, such approaches will
468 not be feasible for an irregular H-NS–DNA nucleoprotein filament. Single-particle methods
469 using H-NS bound to short DNAs such as the *bgl* DRE may be a more feasible approach.

470 **Limitations of the study**

471 Our TEN-map results are limited to a single DNA fragment from the *E. coli bgl* operon for
472 which transcriptional silencing is well characterized and our analysis of footprinting results
473 includes only this fragment and several others from published studies. These fragments are
474 unlikely to represent the full range of possible H-NS DBD contacts on DNAs. Further, our
475 statistical and molecular dynamic modeling of ·OH protection and cleavage is necessarily
476 probabilistic and does not include a full H-NS–DNA filament structure, which remains unknown.
477 Our results thus provide a useful model that requires further testing. The challenges now are to
478 translate this understanding to molecular resolution structures of these filament conformations
479 and to develop approaches that can distinguish locations of linear *versus* bridged filaments in
480 living cells.
481

482 **MATERIALS AND METHODS**

483 **Materials**

484 Reagents were obtained from ThermoFisher (Waltham, MA, USA) or Sigma-Aldrich (St. Louis,
485 MO, USA), unless otherwise specified. Oligonucleotides (Table S2) were obtained from IDT
486 (Coralville, IA); ribonucleotide triphosphates (rNTPs), from Promega (Madison, WI); [α-^{32}P]GTP
487 and [γ-^{32}P]ATP, from Perkin Elmer (Waltham, MA); polyethyleneimine (PEI, avg. MW =
488 60,000), from Acros Organics;
489 (S)-1-(p-Bromoacetamidobenzyl)ethylenediaminetetraacetate (BABE), from Santa Cruz
490 Biotechnology; and DNA-modifying enzymes, from New England Biolabs (NEB; Ipswich, MA).

491 **Plasmid preparation**

492 An expression plasmid for wild type H-NS (pWTHNS) was constructed by Gibson assembly
493 using NEB HiFi reagents (Table S3). The *hns* coding sequence was amplified from *E. coli*
494 MG1655 genomic DNA using primers #11779 and #11780 (Table S2) and the pET21d backbone
495 was amplified from pHNS using primers #11781 and #11782 before assembly. To introduce
496 point mutations in pWTHNS or pHisHNS (Table S3), single primer site-directed mutagenesis
497 was performed with Q5 DNA polymerase (NEB) and primer #8964 to change the Cys21 codon
498 (TGT) to a Ser (AGT) in pHNSC21S. To create pHNSC21SE102C, primer #8964 was used to
499 mutate the Cys21 codon and #8963 was used to change the Gln102 codon (GAA) to Cys (TGT).
500 Sequences of all plasmids were confirmed in key regions by Sanger sequencing.

501 **Protein Purification**

502 Native StpA and Hha were purified as described previously (Boudreau et al., 2018). C-terminally
503 His_{6x}-tagged H-NS was purified as described previously (Kotlajich et al., 2015).
504 *H-NS C21S purification*
505 H-NS C21S was purified as described for non-tagged H-NS in (Boudreau et al., 2018) with the
506 following modifications. Briefly, BL21 λDE3 cells transformed with pHNSC21S and pHiC were
507 grown in 2 L of LB supplemented with ampicillin (100 µg/mL) + gentamycin (10 µg/mL) to
508 OD600 ~0.6 before inducing expression of H-NS C21S with 0.5 mM isopropyl β-D-1-

509 thiogalactopyranoside (IPTG) for 2 h at 37 °C. Pelleted cells were lysed by sonication. H-NS
510 C21S was precipitated with addition of 0.6% (w/v) PEI and eluted with PEI elution buffer
511 containing 0.8 M NaCl followed by ammonium sulfate precipitation. Precipitated H-NS was
512 dissolved in nickel binding buffer and applied to a HisTrap Ni^{2+} column (GE Healthcare).
513 Fractions containing H-NS were mixed with TEV protease to remove the N-terminus His_{6x}-tag.
514 H-NS C21S was reapplied to the nickel column. Non-tagged protein was collected in the flow
515 through and dialyzed against Heparin Buffer (20 mM Tris-HCl pH 7.5, 130 mM NaCl, 100 µM
516 EDTA, 5% glycerol, 1 mM dithiothreitol (DTT)). H-NS C21S was then applied to a HiTrap Hep
517 column (GE Healthcare) and eluted with Heparin Buffer containing 1 M NaCl. Fractions
518 containing H-NS C21S were pooled and dialyzed against Binding Buffer (20 mM Tris-HCl pH
519 7.2, 10% glycerol, 1 mM DTT) supplemented with 130 mM NaCl. To concentrate H-NS, the
520 protein was applied to a Resource Q column (GE Healthcare). The column was washed with a
521 130–200 mM NaCl gradient in Binding Buffer over 7 column volumes. H-NS C21S was eluted
522 in 3 mL Binding Buffer with 500 mM NaCl. Fractions containing H-NS were dialyzed against
523 H-NS Storage Buffer (20 mM Tris-HCl pH 7.5, 0.3 M potassium acetate, 10% glycerol) before
524 storing at -80 °C. Protein purity (~90%) and yield (~5 mg) were determined by SDS-PAGE and
525 Qubit, respectively.
526 *Native WT and C21S E102C H-NS purification*
527 BL21 λDE3 cells were transformed with pWTHNS or pHNSC21SE102C before deleting *hns* by
528 P1 transduction using a lysate from the Δ*hns*::*kan* Keio strain (Coli Genetic Stock Center #9111;
529 (Baba et al., 2006). After confirming the *hns* deletion by PCR, 2 L of cells were grown
530 aerobically in Luria Broth–0.5% NaCl supplemented with 100 µg ampicillin/mL at 37 °C to
531 apparent OD_{600} 0.5 before inducing H-NS expression by addition of IPTG to 1 mM and
532 carbenicillin to 250 µg/mL followed by shaking at 16 h at 25 °C. Cells were pelleted and
533 resuspended in 40 mL of lysis buffer (20 mM Tris-HCl, pH 7.2, 130 mM NaCl, 10% glycerol, 1
534 mM DTT, 1 mM β-mercaptoethanol supplemented with phenylmethylsulfonyl fluoride (PMSF)
535 and protease inhibitor cocktail (PIC; 31.2 mg benzamide/mL, 0.5 mg chymostatin/mL, 0.5 m
536 leupeptin/mL, 0.1 mg pepstatin/mL, 1 mg aprotonin/mL, 1 mg antipain/mL). Cells were lysed by
537 sonication and the lysate was cleared by centrifugation at 27,000 × *g* for 45 min at 4 °C. H-NS

538 containing cell lysate was directly applied to a HiTrap Heparin HP column (GE Healthcare)
539 equilibrated with Binding Buffer with 130 mM NaCl. H-NS was eluted at ~600 mM NaCl using
540 a gradient elution from 130 mM–1 M NaCl over 20 column volumes. Fractions containing H-NS
541 were pooled and dialyzed against binding buffer containing 130 mM NaCl. H-NS was applied to
542 a 1-mL Resource Q column equilibrated with Binding Buffer+130 mM NaCl. Remaining
543 impurities were eluted over a gradient of 130–200 mM NaCl in 10 mL of Binding Buffer. H-NS
544 was eluted with 3 mL of Binding Buffer+500 mM NaCl. Fractions containing H-NS were
545 dialyzed against H-NS Storage Buffer supplemented with 5 mM TCEP. Purity (~90%) and
546 amount of protein (~4 mg) was determined by SDS-PAGE and Qubit analysis, respectively. For
547 tethered cleavage or ·OH cleavage assays, wild-type H-NS was exchanged into a 3x stock of
548 Filament Buffer (3x concentrations: 120 mM HEPES-KOH, pH 8.0, 300 mM potassium
549 glutamate, and 15% glycerol).

550 **FeBABE Conjugation**

551 H-NS C21S and H-NS C21S E102C were exchanged into Conjugation Buffer (10 mM MOPS,
552 pH 8.0, 0.5 mM EDTA, 200 mM NaCl, 5% glycerol) using PD SpinTrap G-25 columns (GE
553 Healthcare #28-9180-04) pre-equilibrated with conjugation buffer. FeBABE was charged by
554 incubating (S)-1-(p-Bromoacetamidobenzyl)ethylenediaminetetraacetate (BABE; Santa Cruz
555 Biotechnology) with $FeCl_3$•$6H_2O$ as previously described (Greiner et al., 1997). H-NS variants
556 (50 µM) were incubated with 10-fold molar excess FeBABE for 2 h at room temperature to
557 conjugate FeBABE to H-NS. After conjugation, 7.6 µmol of conjugated H-NS was combined
558 with 20-fold-molar excess mPEG24 (ThermoFisher # 22713) for an additional 2 h at room
559 temperature. Samples were visualized on 10% Bis-tris gel (ThermoFisher) to determine the
560 percent conjugated (~50% for H-NS C21S E102C). From the remaining conjugation solution,
561 excess FeBABE was removed by applying conjugated H-NS to a clean PD SpinTrap G-25
562 column equilibrated with a 3X stock of Filament Buffer. Conjugation was also confirmed by the
563 appearance of a second, slower migrating band on a 20% polyacryamide PhastGel (GE
564 Healthcare). Fe^{2+}·EDTA–H-NS was stored in aliquots at -80°C and remained stable under these
565 storage conditions for up to 1 year. The DNA-binding activity of the conjugated protein was

566 confirmed by electrophoretic mobility shift assay and by *in vitro* transcription assays described
567 below.

568 **In vitro transcription assay**

569 In vitro transcription of the *bgl* nucleoprotein filament was preformed essentially as described
570 previously (Boudreau et al., 2018; Kotlajich et al., 2015) using 1.5 kb DNA fragment generated
571 by PCR from pMK110 (Haft et al., 2014; Kotlajich et al., 2015) with PCR primers 645 and 3071
572 (Table S2). In brief, 150 nM *E. coli* RNAP (Gribskov and Burgess, 1983; Nayak et al., 2013)
573 reconstituted into holoenzyme with σ^{70} was incubated with a 100 nM DNA containing the λ_{Pr}
574 promoter fused to *bglF–bglG* DNA to form halted elongation complexes (A26 ECs) in 40 mM
575 HEPES-KOH, pH 8.0, 100 mM potassium glutamate, 8 mM magnesium aspartate, 0.022% NP-
576 40, 100 µg acetylated bovine serum albumin/mL, 10% glycerol, 1 mM DTT, 150 µM ApU, 10
577 µM each ATP and UTP, 2.5 µM [α-^{32}P]GTP for 15 min at 37 °C. The halted A26 ECs were then
578 diluted to 10 nM in the same solution plus 100 µg rifampicin/mL and 0.1 U RNasin/µL and
579 incubated with wild-type or modified H-NS at the concentrations indicated in the figures for 20
580 min at 20 °C to form nucleoprotein filaments. Transcription through the filaments at 20 °C was
581 then restarted by adjusting to 4 NTPs to 30 µM each final. Samples were removed at the times
582 indicated, extracted with phenol, ethanol precipitated, and electrophoresed through a 6%
583 polyacryalmide gel (acrylamide:bisacrylamide 19:1) in 8 M urea, 44 mM Tris borate, pH 8.3,
584 1.25 mM EDTA, imaged using a GE Life Sciences Typhoon phosphorimager, and converted to
585 pseudo-densitometry plots as described previously.
586

587 **Electrophoretic mobility shift assay**

588 EMSA was performed as described previously (Boudreau et al., 2018; Kotlajich et al., 2015).
589 Briefly, 1.5 kb *bgl* DNA fragments, which were the same sequence used in in vitro transcription
590 assay, were radiolabeled during PCR. DNA was then incubated with various H-NS proteins as
591 indicated at 20 ˚C to form filaments. Filaments were run on a using 3% polyacrylamide gels at 4
592 °C and imaged using a GE Life Sciences Typhoon phosphorimager.

593 **Tethered-nuclease mapping (TEN-map) Assay**

594 The 146-bp DRE DNA for the TEN-map assay was generated by PCR from a plasmid
595 pMK110 using primers #7486 and #12638 (Tables S2 and S3). To enable visualization by
596 phosphorimaging, one primer was 5′-end-labeled with [γ-^{32}P]ATP prior to the PCR reaction. The
597 PCR product was separated on 5% non-denaturing PAG, eluted from the gel overnight at 4 ˚C in
598 20 mM Tris-HCl pH 7.5, 1 mM EDTA, and 200 mM NaCl, and concentrated using QIAquick gel
599 extraction kit. Increasing concentrations of Fe^{2+}·EDTA–H-NS (from 50 to 5000 nM) were
600 incubated with ~18 nM DRE DNA for 20 min at 20 °C in 7.5 µL of 1X Filament Buffer
601 supplemented with 8 mM magnesium aspartate. Hydroxyl radical cleavage was initiated by
602 addition of 1 µL 2 mM H_2O_2 and 1 µL 2 mM ascorbic acid. Cleavage proceeded for 2 min at 20
603 °C after which 8 µL of the cleavage reaction was added to 100 µL TE-saturated phenol, pH 7.9
604 and 92 µL cleavage stop solution (20 mM EDTA, 20 µg glycogen). The cleavage products were
605 recovered by phenol extraction and ethanol precipitation, and then resuspended in 4 µL
606 formamide stop dye (95% formamide, 20 mM EDTA, 0.02% xylene cyanol, 0.02% bromophenol
607 blue). The samples were electrophoresed through a 7% urea polyacrylamide gel (40.4 x 45.7 cm)
608 in 0.5X TBE and alongside a Maxam-Gilbert A+G ladder for alignment (Maxam and Gilbert,
609 1977) and MspI-digested, ^{32}P-end-labeled pBR322 for size reference. The cleaved DNA was
610 quantified using the densitometric, semi-automated footprinting analysis (SAFA) software (Das
611 et al., 2005). The resulting peak areas were first normalized to total signal in each sample as
612 determined by ImageQuant (version 5.2; GE Lifesciences) analysis of an unsaturated
613 phosphorimage scan of gel and then adjusted to values above and below the average peak area in
614 each sample.

615 For the offset DNA experiment (Figure S5A-B), the TEN-map assay was performed as
616 described above except using a 151-bp DRE DNA amplified from pMK110 using 5′ ^{32}P-end-
617 labeled primer #14374 and unlabeled primer #12386. For the TEN-map assay on the 549-bp
618 DRE fragment (Figure S5C-D), DNA was amplified from pMK110 using 5′ ^{32}P-end-labeled
619 primer #7486 and unlabeled primer #7491. A mixture of Fe^{2+}·EDTA–H-NS and wild-type H-NS
620 at 4:6 ratio and concentration indicated in the figure legend was added to ~18 nM DNA in a 20

621 μL reaction in Filament Buffer supplemented with 0.02% NP-40 and 100 μg acetylated BSA/mL
622 (supplemented Filament Buffer) to compare to the bridged filament cleavage described below.
623 Cleavage was initiated by addition of 1 μL 50 mM ascorbic acid and 4 μL 12.5 mM H_2O_2.
624 Cleavage continued for 2 min at RT before stopping the reaction with 25 μL 22.4 mM thiourea
625 and 20 μL TE. The cleavage products were recovered by phenol extraction and ethanol
626 precipitation, and then resuspended in 4 μL formamide stop dye. The cleavage products were
627 visualized and quantified as described above for the 146-bp DRE DNA. To test the effect of
628 Mg^{2+} on the H-NS DBD location and orientation (Figure 3B and S8), the TEN-map assay was
629 performed on the 549 bp DNA fragment as described except the amount of magnesium aspartate
630 was varied as specified in the figure legend.

631 **Hydroxyl radical footprinting**

632 H-NS filaments were formed on the same 146-bp DRE DNA template used in the TEN-map
633 assay. Concentrations of unmodified H-NS from 50 nM to 4 μM (17–1360 H-NS/kb) were
634 incubated with ~20 nM 5′ ^{32}P-end-labeled DRE DNA in 50 μL reactions in Filament Buffer
635 without glycerol. Filaments were allowed to form at 20 °C for 20 min prior to ·OH cleavage.
636 Cleavage was initiated by addition of 0.6 μL 100 mM ascorbic acid, 4 μL 0.15% H_2O_2, and 6 μL
637 fresh 50 mM Fe^{2+}-EDTA (50 mM $(NH_4)_2Fe(SO_4)_2$, 100 mM EDTA) and incubated for 2 min at
638 20 °C. The no-cleavage control was treated identically except 10.6 μL water was added in place
639 of cleavage reagents. ·OH was then quenched by addition of 80 μL 20 mM thiourea and 60 μL
640 of 0.3 M NaCl, 1 mM EDTA. Cleavage products were recovered by phenol extraction and
641 ethanol precipitation, and then resuspended in 4 μL formamide stop dye. Samples were
642 visualized as described for TEN-map assay and quantified using SAFA (Das et al., 2005).

643 **Bridged H-NS cleavage assay**

644 Bridged H-NS filaments were formed using the previously published bridging pull-down assay
645 (van der Valk et al., 2018; van der Valk et al., 2017) with the following modifications. The 5'
646 ^{32}P-end-labeled, 549-bp DRE DNA (see above) was used as the prey DNA. To form bridged
647 filaments, 5 nM biotinylated 685-bp DNA fragment (68% AT; Table S2) coupled to 3 μL M280
648 streptavidin dynabeads (ThermoFisher) was incubated with 5 nM prey DNA and H-NS in

649 supplemented Filament Buffer at 5–8 μM 6:4 WT H-NS: Fe^{2+}·EDTA–H-NS as indicated in the
650 legend to Figure 3. High levels of H-NS (>5 μM) are required to form bridged filaments in the
651 bridging/pull-down assay, possibly because DNA sequestration on the positively charged
652 streptavidin beads inhibits H-NS binding (Figure 3A; (van der Valk et al., 2017). Bridged
653 filaments were formed for 20 min at 20 °C with shaking at 1000 rpm in an Eppendorf
654 Thermomixer and then separated from unbound protein and DNA using a magnetic rack. Bead-
655 immobilized bridged filaments were then resuspended in 20 μL supplemented Filament Buffer
656 followed by addition of 1 μL 50 mM ascorbic acid and 4 μL 12.5 mM H_2O_2. Cleavage was
657 proceeded for 2 min at RT before addition of 25 μL 22.4 mM thiourea and 20 μL TE. DNA
658 recovered and resuspended in formamide stop dye as described above. The amount of ^{32}P
659 retained on the beads was measured by counting Cerenkov radiation and compared to amounts
660 retained using only unmodified H-NS and prey DNA. Bridging efficiency was calculated as a
661 fraction of total prey DNA ^{32}P that was retained on the beads. Apparent bridging efficiency was
662 likely decreased by some DNA lost during sample processing. Cleavage products were then
663 visualized and quantified by gel electrophoresis and phosphorimaging as described above for the
664 TEN-map assay.

665 **MD simulation of FeBABE-H-NS bound to DNA**

666 Molecular dynamics simulations were run using the program OpenMM (Eastman et al., 2017)
667 with the Charmm36 force field (Best et al., 2012; Hart et al., 2012). Initial setup and post-
668 processing analyses were conducted using the program CHARMM (Brooks et al., 2009). We
669 obtained an initial starting model of H-NS bound to a 12-bp strand of duplex DNA from Vreede
670 and coworkers (Gordon et al., 2011). We "mutated" the side-chain of Cys102 in that model to an
671 FeBABE moiety and generated force field parameters for the organic component of FeBABE by
672 analogy to existing functional groups in the Charmm36 force field. We modeled the Fe^{2+} using a
673 cationic dummy-atom model (Liao et al., 2017). We dissolved the H-NS/FeBABE/DNA system
674 in a cubic box of water with 70 Å edges and added Na^+ and Cl^- ions to reach an ionic strength
675 corresponding to 150 mM with neutral overall charge. The complete system contained 31,518
676 atoms. Following a short geometry optimization, the system was heated from 48 K to 298 K

677 during 1 ns and equilibrated at 298 K and 1 atm for an additional 4 ns prior to production
678 simulations. The simulations employed the NPT ensemble using the Andersen thermostat and
679 MC barostat. Non-bonded interactions were cutoff above a distance of 12 Å with a switching
680 function from 10 Å to 12 Å and the integration time step was 1 fs. We placed a harmonic
681 restraint with force constant of 1 kcal/mol•A^2 on DNA backbone atoms to prevent unraveling at
682 the ends of the duplex, which we observed in initial tests. Under these conditions, we simulated
683 the system for 500 ns, taking snapshots every 10 ps.

684 In each frame, we calculated the distance from the Fe^{2+} to every C5′, because FeBABE-
685 induced cleavage is thought to occur by ·OH radical reacting with C5′-H (Balasubramanian et
686 al., 1998). We modeled the concentration of ·OH radicals at C5′ based on a diffusion model
687 where the concentration of radicals around the Fe^{2+} decays according to a Gaussian distribution
688 (Cheal et al., 2009). To account for cleavage sites that are shielded from solvent by the bound
689 protein, the average concentration of ·OH at each site was scaled linearly by the average solvent
690 accessible surface area of the corresponding C5′ methylene group (Figure 5B). The scaled
691 concentration at each site yields the cleavage propensities displayed in Figure 5A. The
692 simulations used a relatively short 12-bp duplex in order to achieve reasonable computational
693 efficiency and to run simulations long enough to adequately sample the conformational
694 flexibility of the FeBABE. To model cleavage propensities for bp at greater distances from the
695 H-NS binding site, we assumed that long-range interactions with DNA do not influence the
696 overall behavior of FeBABE and thus estimated those cleavage propensities by adding additional
697 DNA to the saved trajectories after the simulation was complete.

698 **Statistical modeling of DBD locations in H-NS filaments**

699 The ·OH footprinting data for each H-NS concentration tested (0–4 μM titration), each strand,
700 and each independent replicate was normalized by dividing the signal in each lane by the average
701 signal within a lane. The resulting ratio was $\log_2$ transformed to center the data at zero. The $\log_2$-
702 normalized deviance from the average signal from each strand was separately fit to a Bayesian
703 multi-level model of the following form:
704
705 $$y_i \sim \text{Student's } t(\mu_i, \sigma, \nu)$$

706 $$\mu_i = \alpha_{\mathrm{bp}[i]} + \beta_{\mathrm{bp}[i]}[\mathrm{HNS}]$$

707 $$\begin{bmatrix}\alpha_{\mathrm{bp}}\\ \beta_{\mathrm{bp}}\end{bmatrix} = \mathrm{MVNormal}\left(\begin{bmatrix}\alpha\\ \beta\end{bmatrix}, \boldsymbol{S}\right)$$

708 $$\boldsymbol{S} = \begin{pmatrix}\sigma_\alpha & 0\\ 0 & \sigma_\beta\end{pmatrix}\boldsymbol{R}\begin{pmatrix}\sigma_\alpha & 0\\ 0 & \sigma_\beta\end{pmatrix}$$

709 $$\boldsymbol{R} = \begin{pmatrix}1 & \rho\\ \rho & 1\end{pmatrix}$$

710 With the following weakly regularizing priors:

711 $$\alpha \sim \mathrm{Normal}(0, 10)$$

712 $$\beta \sim \mathrm{Normal}(0, 10)$$

713 $$\sigma \sim \mathrm{HalfCauchy}(0, 1)$$

714 $$\sigma_\alpha \sim \mathrm{HalfCauchy}(0, 1)$$

715 $$\sigma_\beta \sim \mathrm{HalfCauchy}(0, 1)$$

716 $$\boldsymbol{R} \sim \mathrm{LKJcorr}(2)$$

717 The models were fit using the R package brms (version 2.10.0) (Bürkner, 2017) and default
718 priors were used for any parameter for which a prior is not specified above.

719 Similarly, the tethered-cleavage data for each concentration (0–3 μM titration) was
720 normalized by first dividing each lane by a constant factor resulting from quantification of a
721 short scan of the entire lane. The data was then centered by subtracting the average signal within
722 each lane. The centered and normalized signal for each strand separately was then fit to a
723 Bayesian multilevel, of the form described above, with the following priors:

724 $$\alpha \sim \mathrm{Normal}(0, 0.1)$$

725 $$\beta \sim \mathrm{Normal}(0, 0.1)$$

726 Default priors were used for every parameter not specified above. Notably, the 4 μM and 5 μM
727 concentrations were not included in the tethered cleavage fits due to their substantial deviance
728 from linearity. Point estimates for each slope at each bp in the models above were estimated
729 from the average of the posterior distribution for that slope. These estimates can be interpreted as
730 the H-NS concentration-dependent change in signal at each bp with data-driven shrinkage
731 towards the grand mean of slopes for every bp.

732 To match the MD simulations with the *in vitro* data, the slope estimates for each strand in
733 each data type were Robust-Z normalized using the following formula:

734 $$y_{\text{scaled}} = \frac{y - \text{median}(y)}{1.4826 \times \text{MAD}(y)}$$

735 where MAD is the median absolute deviation and 1.4826 is a scaling factor to convert the MAD
736 to an estimate for the standard deviation (Hampel, 1974; Rousseeuw and Croux, 1993).
737 Similarly, the expected 15-bp cleavage pattern of a single H-NS DBD (Figure 5A) was also
738 scaled to a standard Normal using the formula above. Using a sliding window, the Manhattan
739 distance between the scaled, tethered-cleavage estimates and the scaled, 15-bp expected cleavage
740 pattern was calculated for each base centered on the sixth bp of the cleavage pattern (triangle in
741 Figure 5). Due to the asymmetry of the expected cleavage pattern, we performed this calculation
742 in both directions along the DNA corresponding to two different possible orientations of the H-
743 NS DNA binding domain. Since this score is a distance, lower values indicate a closer match
744 between the expected cleavage pattern and the tethered cleavage data.

745 To assess the statistical significance of the MD match scores, we performed a one-sided
746 Monte Carlo permutation test by considering the MD match score at each base pair in 1000
747 different random shuffles of the tethered-cleavage data for each direction of the H-NS DBD. We
748 generated a *p*-value by determining the fraction of shuffled datasets that had a match score
749 greater than or equal to the match score with unshuffled data. We considered MD match scores
750 below the 5th percentile of the random MD match scores (p-value < 0.05) to signify a statistically
751 significant match between the expected cleavage pattern and the tethered cleavage data.

752 To determine possible localizations of the H-NS DBD in the ·OH footprinting data, we
753 performed the same procedure described above using the solvent accessibility of the 5′ carbon of
754 the DNA duplex as the expected pattern of protection imparted by the H-NS DBD (Figure 5B)
755 and matched that pattern to the ·OH footprinting data (Figure 5F,H).

756 To combine evidence for the DBD locations between the footprinting and TEN-map
757 datasets (Figure 6) we used Fisher's method (Heard and Rubin-Delanchy, 2018) to generate
758 combined *p*-values for each base pair and DBD orientation.

759 **Predicting H-NS DBD binding locations**

760 To predict H-NS DBD binding a dataset consisting of sequence, structural, and electrostatic
761 parameters was generated. **Sequence –** For each bp, the following sequence features were
762 generated: the A/T content of a 5bp window centered on the bp (A/T content-5p), overlap with a
763 4mer matching the criteria for an AT tract, overlap with a 4mer matching the criteria for a TA
764 step, and overlap with a motif match to the Lang et al. H-NS PWM (Lang et al., 2007). Motif
765 matches were generated by running FIMO (version 5.05) (Grant et al., 2011) over the P-*bgl*
766 fragment using a third-order Markov background model trained on the *E. coli* genome, searching
767 on both strands, and using a *p*-value cutoff of 0.001 with no FDR correction. **Structure and**
768 **electrostatics -** DNA structure and electrostatic features were generated using the DNAshapeR
769 package (Chiu et al., 2016) using default parameters on the P-*bgl* fragment.

770 To predict the locations of H-NS DBD binding at the base-pair level, a LASSO logistic
771 regression model was trained on the H-NS TEN-map and footprinting data using glmnet version
772 2.0-16 (Friedman et al., 2010b). For these models, we assigned as bound by H-NS base pairs for
773 which the *p*-value for a match to the predicted patterns (Figures 5C,D and S12) was less than
774 0.05 for either the TEN-map or the footprinting data in either orientation (position 106 was
775 excluded from the LASSO model). All continuous features were centered by their average and
776 scaled by their standard deviation before training. The LASSO model reveals the minimal set of
777 DNA features needed for the prediction of a given dataset by only including non-zero
778 coefficients for a feature if that feature provides independent information from other non-zero
779 coefficients already present in the model. Since all input data was centered and scaled before
780 training the model, the relative magnitude of each coefficient can be interpreted as the
781 importance for that feature in predicting the outcome, with positive values indicating an increase
782 in the probability of a region being bound by a protein when the associated feature is a higher
783 value and negative values indicating the opposite. Models were trained using 10-fold cross-
784 validation with stratified sampling and the penalty parameter, λ, set as one standard error away
785 from the minimum binomial deviance. λ was determined individually for each subsampled
786 dataset using 10-fold cross-validation internally to test for sensitivity to the exact data used to

train the model. Predictive performance was assessed using a model trained on the full data set with 10-fold cross-validation used to determine the λ parameter.

ACKNOWLEDGEMENTS

We thank Jocelyne Vreede (University of Amsterdam) for sharing coordinates for an H-NS DBD–DNA structure and for modeling FeBABE into the structure. We thank members of the Landick lab for many helpful discussions and comments on this manuscript. This work was supported by NIH grant GM38660 to R.L. B.A.S. was supported by an NSF Graduate Research Fellowship (DGE-1256259). C.M.H. was supported by an NSF Graduate Research Fellowship (DGE-1747503) and an NIH Chemical Biology Interface Training grant (T32 GM008505). Computational resources for MD simulations were provided by the Extreme Science and Engineering Discovery Environment (XSEDE; allocation TG-MCB180084 to D.R.), which is supported by National Science Foundation grant number ACI-1548562.

802 **REFERENCES**

803 Arold, S.T., Leonard, P.G., Parkinson, G.N., and Ladbury, J.E. (2010). H-NS forms a
804 superhelical protein scaffold for DNA condensation. PNAS *107*, 15728-15732.
805 10.1073/pnas.1006966107.

806 Baba, T., Ara, T., Hasegawa, M., Takai, Y., Okumura, Y., Baba, M., Datsenko, K.A., Tomita,
807 M., Wanner, B.L., and Mori, H. (2006). Construction of Escherichia coli K-12 in-frame,
808 single-gene knockout mutants: the Keio collection. Mol Syst Biol *2*, 2006.0008.
809 10.1038/msb4100050.

810 Balasubramanian, B., Pogozelski, W.K., and Tullis, T.D. (1998). DNA strand breaking by the
811 hydroxyl radical is governed by the accessible surface area of the hydrogen atoms of the DNA
812 backbone. Proceedings of the National Academy of Sciences, USA *95*, 9738-9743.
813 10.1073/pnas.95.17.9738.

814 Bansal, M., Bhattacharyya, D., and Ravi, B. (1995). NUPARM and NUCGEN: software for
815 analysis and generation of sequence dependent nucleic acid structures. Comput Appl Biosci
816 *11*, 281-287. 10.1093/bioinformatics/11.3.281.

817 Best, R.B., Zhu, X., Shim, J., Lopes, P.E.M., Mittal, J., Feig, M., and MacKerell, A.D. (2012).
818 Optimization of the Additive CHARMM All-Atom Protein Force Field Targeting Improved
819 Sampling of the Backbone phi, psi and Side-Chain chi(1) and chi(2) Dihedral Angles. Journal
820 of Chemical Theory and Computation *8*, 3257-3273. 10.1021/ct300400x.

821 Boudreau, B.A., Hron, D.R., Qin, L., van der Valk, R.A., Kotlajich, M.V., Dame, R.T., and
822 Landick, R. (2018). StpA and Hha stimulate pausing by RNA polymerase by promoting
823 DNA-DNA bridging of H-NS filaments. Nucleic Acids Res *46*, 5525-5546.
824 10.1093/nar/gky265.

825 Bouffartigues, E., Buckle, M., Badaut, C., Travers, A., and Rimsky, S. (2007). H-NS cooperative
826 binding to high-affinity sites in a regulatory element results in transcriptional silencing.
827 Nature structural & molecular biology *14*, 441-448. 10.1038/nsmb1233.

828 Brooks, B.R., Brooks, C.L., Mackerell, A.D., Nilsson, L., Petrella, R.J., Roux, B., Won, Y.,
829 Archontis, G., Bartels, C., Boresch, S.*, et al.* (2009). CHARMM: The Biomolecular
830 Simulation Program. Journal of Computational Chemistry *30*, 1545-1614. 10.1002/Jcc.21287.

831 Burkhoff, A.M., and Tullis, T.D. (1988). Structural details of an adenine tract that does not cause
832 DNA to bend. Nature *331*, 455-457. 10.1038/331455a0.

833 Bürkner, P.-C. (2017). brms: An R Package for Bayesian Multilevel Models Using Stan. Journal
834 of Statistical Software *80*. 10.18637/jss.v080.i01.

835 Chandraprakash, D., and Seshasayee, A.S.N. (2014). Inhibition of factor-dependent transcription
836 termination in Escherichia coli might relieve xenogene silencing by abrogating H-NS-DNA
837 interactions in vivo. Journal of Biosciences *39*, 53-61. 10.1007/s12038-014-9413-4.

838 Cheal, S.M., Ng, M., Barrios, B., Miao, Z., Kalani, A.K., and Meares, C.F. (2009). Mapping
839 protein-protein interactions by localized oxidation: consequences of the reach of hydroxyl
840 radical. Biochemistry *48*, 4577-4586. 10.1021/bi900273j.

841 Chiu, T.-P., Rao, S., Mann, R.S., Honig, B., and Rohs, R. (2017). Genome-wide prediction of
842 minor-groove electrostatic potential enables biophysical modeling of protein–DNA binding.
843 Nucleic Acids Research *45*, 12565-12576. 10.1093/nar/gkx915.

844 Chiu, T.P., Comoglio, F., Zhou, T., Yang, L., Paro, R., and Rohs, R. (2016). DNAshapeR: an
845 R/Bioconductor package for DNA shape prediction and feature encoding. Bioinformatics *32*,
846 1211-1213. 10.1093/bioinformatics/btv735.

847 Cook, P.R., and Marenduzzo, D. (2018). Transcription-driven genome organization: a model for
848 chromosome structure and the regulation of gene expression tested through simulations.
849 Nucleic Acids Research *46*, 9895-9906. 10.1093/nar/gky763.

850 Dame, R.T., Noom, M.C., and Wuite, G.J. (2006). Bacterial chromatin organization by H-NS
851 protein unravelled using dual DNA manipulation. Nature *444*, 387-390. 10.1038/nature05283.

852 Dame, R.T., Rashid, F.M., and Grainger, D.C. (2020). Chromosome organization in bacteria:
853 mechanistic insights into genome structure and function. Nat Rev Genet. 10.1038/s41576-
854 019-0185-4.

855 Dame, R.T., Wyman, C., and Goosen, N. (2000). H-NS mediated compaction of DNA visualised
856 by atomic force microscopy. Nucleic Acids Res *28*, 3504-3510. 10.1093/nar/28.18.3504.

857 Dame, R.T., Wyman, C., Wurm, R., Wagner, R., and Goosen, N. (2002). Structural basis for H-
858 NS-mediated trapping of RNA polymerase in the open initiation complex at the rrnB P1. J
859 Biol Chem *277*, 2146-2150. 10.1074/jbc.C100603200.

860 Das, R., Laederach, A., Pearlman, S.M., Herschlag, D., and Altman, R.B. (2005). SAFA: semi-
861 automated footprinting analysis software for high-throughput quantification of nucleic acid
862 footprinting experiments. RNA *11*, 344-354. 10.1261/rna.7214405.

863 Dole, S., Nagarajavel, V., and Schnetz, K. (2004). The histone-like nucleoid structuring protein
864 H-NS represses the Escherichia coli bgl operon downstream of the promoter. Mol Microbiol
865 *52*, 589-600. 10.1111/j.1365-2958.2004.04001.x.

866 Eastman, P., Swails, J., Chodera, J.D., McGibbon, R.T., Zhao, Y.T., Beauchamp, K.A., Wang,
867 L.P., Simmonett, A.C., Harrigan, M.P., Stern, C.D.*, et al.* (2017). OpenMM 7: Rapid
868 development of high performance algorithms for molecular dynamics. PLoS Comput Biol *13*,
869 17. 10.1371/journal.pcbi.1005659.

870 Friedman, J., Hastie, T., and Tibshirani, R. (2010a). Regularization Paths for Generalized Linear
871 Models via Coordinate Descent. J Stat Softw *33*, 1-22.

872 Friedman, J.H., Hastie, T., and Tibshirani, R. (2010b). Regularization Paths for Generalized
873 Linear Models via Coordinate Descent. 2010 *33*, Journal of Statistical Software.
874 10.18637/jss.v033.i01.

875 Gao, Y., Foo, Y.H., Winardhi, R.S., Tang, Q., Yan, J., and Kenney, L.J. (2017). Charged
876 residues in the H-NS linker drive DNA binding and gene silencing in single cells. Proceedings
877 of the National Academy of Sciences of the United States of America *114*, 12560-12565.
878 10.1073/pnas.1716721114.

879 Gawade, P., Gunjal, G., Sharma, A., and Ghosh, P. (2020). Reconstruction of transcriptional
880 regulatory networks of Fis and H-NS in Escherichia coli from genome-wide data analysis.
881 Genomics *112*, 1264-1272. 10.1016/j.ygeno.2019.07.013.

882 Gordon, B.R., Li, Y., Cote, A., Weirauch, M.T., Ding, P., Hughes, T.R., Navarre, W.W., Xia, B.,
883 and Liu, J. (2011). Structural basis for recognition of AT-rich DNA by unrelated xenogeneic
884 silencing proteins. Proceedings of the National Academy of Sciences of the United States of
885 America *108*, 10690-10695. 10.1073/pnas.1102544108.

886 Grainger, D.C. (2016). Structure and function of bacterial H-NS protein. Biochem Soc Trans *44*,
887 1561-1569. 10.1042/BST20160190.

888 Grainger, D.C., Hurd, D., Goldberg, M.D., and Busby, S.J. (2006). Association of nucleoid
889 proteins with coding and non-coding segments of the Escherichia coli genome. Nucleic Acids
890 Res *34*, 4642-4652. 10.1093/nar/gkl542.

891 Grant, C.E., Bailey, T.L., and Noble, W.S. (2011). FIMO: scanning for occurrences of a given
892 motif. Bioinformatics *27*, 1017-1018. 10.1093/bioinformatics/btr064.

893 Greiner, D.P., Miyake, R., Moran, J.K., Jones, A.D., Negishi, T., Ishihama, A., and Meares, C.F.
894 (1997). Synthesis of the protein cutting reagent Iron (*S*)-1-(*p*-
895 Bromoacetamidobenzyl)ethylenediaminetetraacetate and conjugation to cysteine side chains.
896 Bioconjugate Chemistry *8*, 44-48. 10.1021/bc9600731.

897 Gribskov, M., and Burgess, R.R. (1983). Overexpression and purification of the sigma subunit of
898 Escherichia coli RNA polymerase. Gene *26*, 109-118. 10.1016/0378-1119(83)90180-4.

899 Gulvady, R., Gao, Y., Kenney, L.J., and Yan, J. (2018). A single molecule analysis of H-NS
900 uncouples DNA binding affinity from DNA specificity. Nucleic Acids Res *46*, 10216-10224.
901 10.1093/nar/gky826.

902 Haft, R.J., Keating, D.H., Schwaegler, T., Schwalbach, M.S., Vinokur, J., Tremaine, M., Peters,
903 J.M., Kotlajich, M.V., Pohlmann, E.L., Ong, I.M.*, et al.* (2014). Correcting direct effects of
904 ethanol on translation and transcription machinery confers ethanol tolerance in bacteria.
905 Proceedings of the National Academy of Sciences of the United States of America *111*,
906 E2576-2585. 10.1073/pnas.1401853111.

907 Hampel, F.R. (1974). The Influence Curve and its Role in Robust Estimation. Journal of the
908 American Statistical Association *69*, 383-393. 10.1080/01621459.1974.10482962.

909 Hart, K., Foloppe, N., Baker, C.M., Denning, E.J., Nilsson, L., and MacKerell, A.D. (2012).
910 Optimization of the CHARMM Additive Force Field for DNA: Improved Treatment of the
911 BI/BII Conformational Equilibrium. Journal of Chemical Theory and Computation *8*, 348-
912 362. 10.1021/ct200723y.

913 Heard, N.A., and Rubin-Delanchy, P. (2018). Choosing between methods of combining p-values.
914 Biometrika *105*, 239-246. 10.1093/biomet/asx076.

915 Jumper, J., Evans, R., Pritzel, A., Green, T., Figurnov, M., Ronneberger, O., Tunyasuvunakool,
916 K., Bates, R., Zidek, A., Potapenko, A.*, et al.* (2021). Highly accurate protein structure
917 prediction with AlphaFold. Nature *596*, 583-589. 10.1038/s41586-021-03819-2.

918 Kahramanoglou, C., Seshasayee, A.S., Prieto, A.I., Ibberson, D., Schmidt, S., Zimmermann, J.,
919 Benes, V., Fraser, G.M., and Luscombe, N.M. (2011). Direct and indirect effects of H-NS and
920 Fis on global gene expression control in Escherichia coli. Nucleic Acids Res *39*, 2073-2091.
921 10.1093/nar/gkq934.

922 Kotlajich, M.V., Hron, D.R., Boudreau, B.A., Sun, Z., Lyubchenko, Y.L., and Landick, R.
923 (2015). Bridged filaments of histone-like nucleoid structuring protein pause RNA polymerase
924 and aid termination in bacteria. Elife *4*. 10.7554/eLife.04970.

925 Lang, B., Blot, N., Bouffartigues, E., Buckle, M., Geertz, M., Gualerzi, C.O., Mavathur, R.,
926 Muskhelishvili, G., Pon, C.L., Rimsky, S.*, et al.* (2007). High-affinity DNA binding sites for
927 H-NS provide a molecular basis for selective silencing within proteobacterial genomes.
928 Nucleic Acids Res *35*, 6330-6337. 10.1093/nar/gkm712.

929 Liao, Q.H., Pabis, A., Strodel, B., and Kamerlin, S.C.L. (2017). Extending the Nonbonded
930 Cationic Dummy Model to Account for Ion-Induced Dipole Interactions. Journal of Physical
931 Chemistry Letters *8*, 5408-5414. 10.1021/acs.jpclett.7b02358.

932 Liu, Y., Chen, H., Kenney, L.J., and Yan, J. (2010). A divalent switch drives H-NS/DNA-
933 binding conformations between stiffening and bridging modes. Genes Dev *24*, 339-344.
934 10.1101/gad.1883510.

935 Lucchini, S., Rowley, G., Goldberg, M.D., Hurd, D., Harrison, M., and Hinton, J.C. (2006). H-
936 NS mediates the silencing of laterally acquired genes in bacteria. PLoS Pathog *2*, e81.
937 10.1371/journal.ppat.0020081.

938 Lucht, J.M., Dersch, P., Kempf, B., and Bremer, E. (1994). Interactions of the nucleoid-
939 associated DNA-binding protein H-NS with the regulatory region of the osmotically
940 controlled proU operon of Escherichia coli. J Biol Chem *269*, 6578-6578.

941 Luger, K., Mader, A.W., Richmond, R.K., Sargent, D.F., and Richmond, T.J. (1997). Crystal
942 structure of the nucleosome core particle at 2.8 Å resolution. Nature *389*, 251-260.
943 10.1038/38444.

944 Maxam, A.M., and Gilbert, W. (1977). A new method for sequencing DNA. Proceedings of the
945 National Academy of Sciences, USA *74*, 560-564. 10.1073/pnas.74.2.560.

946 Moreira, R.N., Dressaire, C., Domingues, S., and Arraiano, C.M. (2011). A new target for an old
947 regulator: H-NS represses transcription of bolA morphogene by direct binding to both
948 promoters. Biochem Biophys Res Commun *411*, 50-55. 10.1016/j.bbrc.2011.06.084.

949 Murakami, K., Kimura, M., Owens, J.T., Meares, C.F., and Ishihama, A. (1997). The two alpha
950 subunits of Escherichia coli RNA polymerase are asymmetrically arranged and contact
951 different halves of the DNA upstream element. Proceedings of the National Academy of
952 Sciences of the United States of America *94*, 1709-1714. 10.1073/pnas.94.5.1709.

953 Nagarajavel, V., Madhusudan, S., Dole, S., Rahmouni, A.R., and Schnetz, K. (2007). Repression
954 by binding of H-NS within the transcription unit. J Biol Chem *282*, 23622-23630.
955 10.1074/jbc.M702753200.

956 Navarre, W.W., Porwollik, S., Wang, Y., McClelland, M., Rosen, H., Libby, S.J., and Fang, F.C.
957 (2006). Selective silencing of foreign DNA with low GC content by the H-NS protein in
958 Salmonella. Science *313*, 236-238. 10.1126/science.1128794.

959 Nayak, D., Voss, M., Windgassen, T., Mooney, R.A., and Landick, R. (2013). Cys-pair reporters
960 detect a constrained trigger loop in a paused RNA polymerase. Mol Cell *50*, 882-893.
961 10.1016/j.molcel.2013.05.015.

962 Peters, J.M., Mooney, R.A., Grass, J.A., Jessen, E.D., Tran, F., and Landick, R. (2012). Rho and
963 NusG suppress pervasive antisense transcription in Escherichia coli. Genes Dev *26*, 2621-
964 2633. 10.1101/gad.196741.112.

965 Qin, L., Bdira, F.B., Sterckx, Y.G.J., Volkov, A.N., Vreede, J., Giachin, G., van Schaik, P.,
966 Ubbink, M., and Dame, R.T. (2020). Structural basis for osmotic regulation of the DNA
967 binding properties of H-NS proteins. Nucleic Acids Res *48*, 2156-2172. 10.1093/nar/gkz1226.

968 Qin, L., Erkelens, A.M., Ben Bdira, F., and Dame, R.T. (2019). The architects of bacterial DNA
969 bridges: a structurally and functionally conserved family of proteins. Open Biol *9*, 190223.
970 10.1098/rsob.190223.

971 Rana, T.M., and Meares, C.F. (1991). Transfer of oxygen from an artificial protease to peptide
972 carbon during proteolysis. Proceedings of the National Academy of Sciences of the United
973 States of America *88*, 10578-10582. 10.1073/pnas.88.23.10578.

974 Riccardi, E., van Mastbergen, E.C., Navarre, W.W., and Vreede, J. (2019). Predicting the
975 mechanism and rate of H-NS binding to AT-rich DNA. PLoS Comput Biol *15*, e1006845.
976 10.1371/journal.pcbi.1006845.

977 Rousseeuw, P.J., and Croux, C. (1993). Alternatives to the Median Absolute Deviation. Journal
978 of the American Statistical Association *88*, 1273-1283. 10.1080/01621459.1993.10476408.

979 Sankar, T.S., Neelakanta, G., Sangal, V., Plum, G., Achtman, M., and Schnetz, K. (2009). Fate of
980 the H-NS-repressed bgl operon in evolution of Escherichia coli. PLoS genetics *5*, e1000405.
981 10.1371/journal.pgen.1000405.

982 Saxena, S., and Gowrishankar, J. (2011). Modulation of Rho-Dependent Transcription
983 Termination in *Escherichia coli* by the H-NS Family of Proteins. Journal of Bacteriology *193*,
984 3832. 10.1128/JB.00220-11.

985 Shahul Hameed, U.F., Liao, C., Radhakrishnan, A.K., Huser, F., Aljedani, S.S., Zhao, X.,
986 Momin, A.A., Melo, F.A., Guo, X., Brooks, C., *et al.* (2018). H-NS uses an autoinhibitory
987 conformational switch for environment-controlled gene silencing. Nucleic Acids Res.
988 10.1093/nar/gky1299.

989 Shen, B.A., and Landick, R. (2019). Transcription of bacterial chromatin. J Mol Biol.
990 10.1016/j.jmb.2019.05.041.

991 Shin, M., Song, M., Rhee, J.H., Hong, Y., Kim, Y.J., Seok, Y.J., Ha, K.S., Jung, S.H., and Choy,
992 H.E. (2005). DNA looping-mediated repression by histone-like protein H-NS: specific
993 requirement of Esigma70 as a cofactor for looping. Genes Dev *19*, 2388-2398.
994 10.1101/gad.1316305.

995 Singh, S.S., and Grainger, D.C. (2013). H-NS can facilitate specific DNA-binding by RNA
996 polymerase in AT-rich gene regulatory regions. PLoS genetics *9*, e1003589.
997 10.1371/journal.pgen.1003589.

998 Srinivasan, R., Chandraprakash, D., Krishnamurthi, R., Singh, P., Scolari, V.F., Krishna, S., and
999 Seshasayee, A.S. (2013). Genomic analysis reveals epistatic silencing of "expensive" genes in
1000 Escherichia coli K-12. Mol Biosyst *9*, 2021-2033. 10.1039/c3mb70035f.

1001 Talbert, P.B., Meers, M.P., and Henikoff, S. (2019). Old cogs, new tricks: the evolution of gene
1002 expression in a chromatin context. Nat Rev Genet *20*, 283-297. 10.1038/s41576-019-0105-7.

1003 Ulissi, U., Fabbretti, A., Sette, M., Giuliodori, A.M., and Spurio, R. (2014). Time-resolved
1004 assembly of a nucleoprotein complex between Shigella flexneri virF promoter and its
1005 transcriptional repressor H-NS. Nucleic Acids Res *42*, 13039-13050. 10.1093/nar/gku1052.

1006 van der Valk, R.A., Qin, L., Moolenaar, G.F., and Dame, R.T. (2018). Quantitative
1007 Determination of DNA Bridging Efficiency of Chromatin Proteins. Methods Mol Biol *1837*,
1008 199-209. 10.1007/978-1-4939-8675-0_12.

1009 van der Valk, R.A., Vreede, J., Qin, L., Moolenaar, G.F., Hofmann, A., Goosen, N., and Dame,
1010 R.T. (2017). Mechanism of environmentally driven conformational changes that modulate H-
1011 NS DNA-bridging activity. Elife *6*, e27369. 10.7554/eLife.27369.

1012 Will, W.R., Bale, D.H., Reid, P.J., Libby, S.J., and Fang, F.C. (2015). Evolutionary expansion of
1013 a regulatory network by counter-silencing. Nat Commun *5*, 5270. 10.1038/ncomms6270.

1014 Will, W.R., Whitham, P.J., Reid, P.J., and Fang, F.C. (2018). Modulation of H-NS
1015 transcriptional silencing by magnesium. Nucleic Acids Res *46*, 5717-5725.
1016 10.1093/nar/gky387.

1017 Zhao, X., Remington, J.M., Schneebeli, S.T., Arold, S.T., and Li, J. (2021a). Molecular Basis for
1018 Environment Sensing by a Nucleoid-Structuring Bacterial Protein Filament. J Phys Chem Lett
1019 *12*, 7878-7884. 10.1021/acs.jpclett.1c01710.

1020 Zhao, X., Shahul Hameed, U.F., Kharchenko, V., Liao, C., Huser, F., Remington, J.M.,
1021 Radhakrishnan, A.K., Jaremko, M., Jaremko, L., Arold, S.T*., et al.* (2021b). Molecular basis
1022 for the adaptive evolution of environment-sensing by H-NS proteins. Elife *10*.
1023 10.7554/eLife.57467.

1024 Zhou, T., Yang, L., Lu, Y., Dror, I., Dantas Machado, A.C., Ghane, T., Di Felice, R., and Rohs,
1025 R. (2013). DNAshape: a method for the high-throughput prediction of DNA structural
1026 features on a genomic scale. Nucleic Acids Res *41*, W56-62. 10.1093/nar/gkt437.

1027

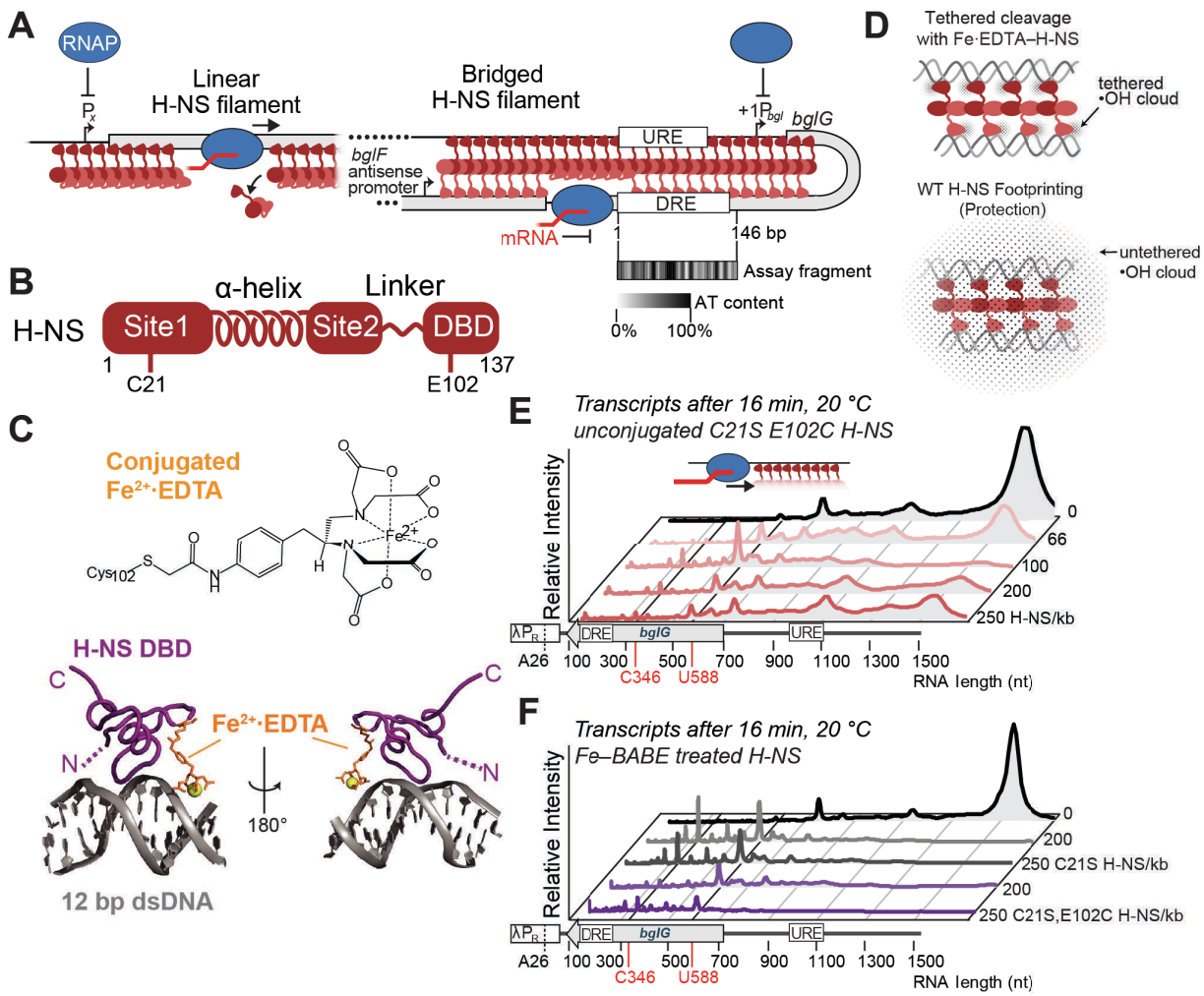

Figure 1. H-NS tethered to Fe^{2+}·EDTA forms bridged filaments that stimulate pausing by RNA polymerase.

(A) Mechanisms of gene silencing by H-NS illustrated for the *E. coli bgl* operon. Linear and bridged H-NS filaments (dark and light red monomers) can block RNAP (blue) from binding to promoters whereas only bridged H-NS can inhibit elongation of RNAP by stimulating pausing (Dame et al., 2002; Kotlajich et al., 2015; Shin et al., 2005; Singh 2013). AT-rich, high affinity–binding sites nucleate filament formation at the *bgl* upstream and downstream regulatory elements (URE and DRE) (Dole et al., 2004). The AT-content of the 146-bp DRE DNA fragment used in the TEN-map assay is shown using a gray-scale heat map.

(B) Structure of the H-NS monomer. Sites 1 and 2 in the N-terminal oligomerization domain, connected by a flexible α-helix, make head–head, tail–tail contacts in H-NS–DNA filaments (Shahul Hameed et al., 2018; van der Valk et al., 2017). A 15-aa flexible linker connects the C-terminal DBDs to the tail–tail junction (Gao et al., 2017). Substitutions (C21S, E102C) enabling Fe^{2+}·EDTA conjugation are indicated.

(C) Model of the H-NS DBD (PDB 2L93) bound to 12-bp duplex DNA (Riccardi et al., 2019) with Fe^{2+}·EDTA tethered to position 102.

(D) Comparison of ·OH generated in TEN-map (top) vs. ·OH footprinting (bottom) assays.

(E) Pseudo-densitometry traces of RNA transcripts formed by RNAP at 20 °C and 30 μM NTP on a 1.5 kb *bgl* DNA 16 min after release from a λP_R promoter–A26 halt site with no H-NS (top) or 66–250 C21S, E102C H-NS monomer/kb DNA. Peaks represent paused RNAP (e.g., at positions 346 and 588) or run-off transcript (1538 nt) (Kotlajich et al., 2015). At ~50 to ~150 monomer/kb, H-NS forms bridged filaments that stimulate pausing whereas higher concentrations of H-NS saturate DBD binding sites in linear filaments (Boudreau et al., 2018; Kotlajich et al., 2015). Bridged and linear filament formation was verified by EMSA (Figure S2). See also Figure S1 for transcription results using wild-type H-NS and Figure S3 for sequence of *bgl* DRE.

(F) RNA transcripts formed in the same assay as panel E but using control C21S H-NS and C21S, E102C H-NS treated with FeBABE. Fe^{2+}·EDTA–H-NS formed by C21S, E102C H-NS contained Fe^{2+}·EDTA conjugated to ~50% of the E102C thiols (see Methods).

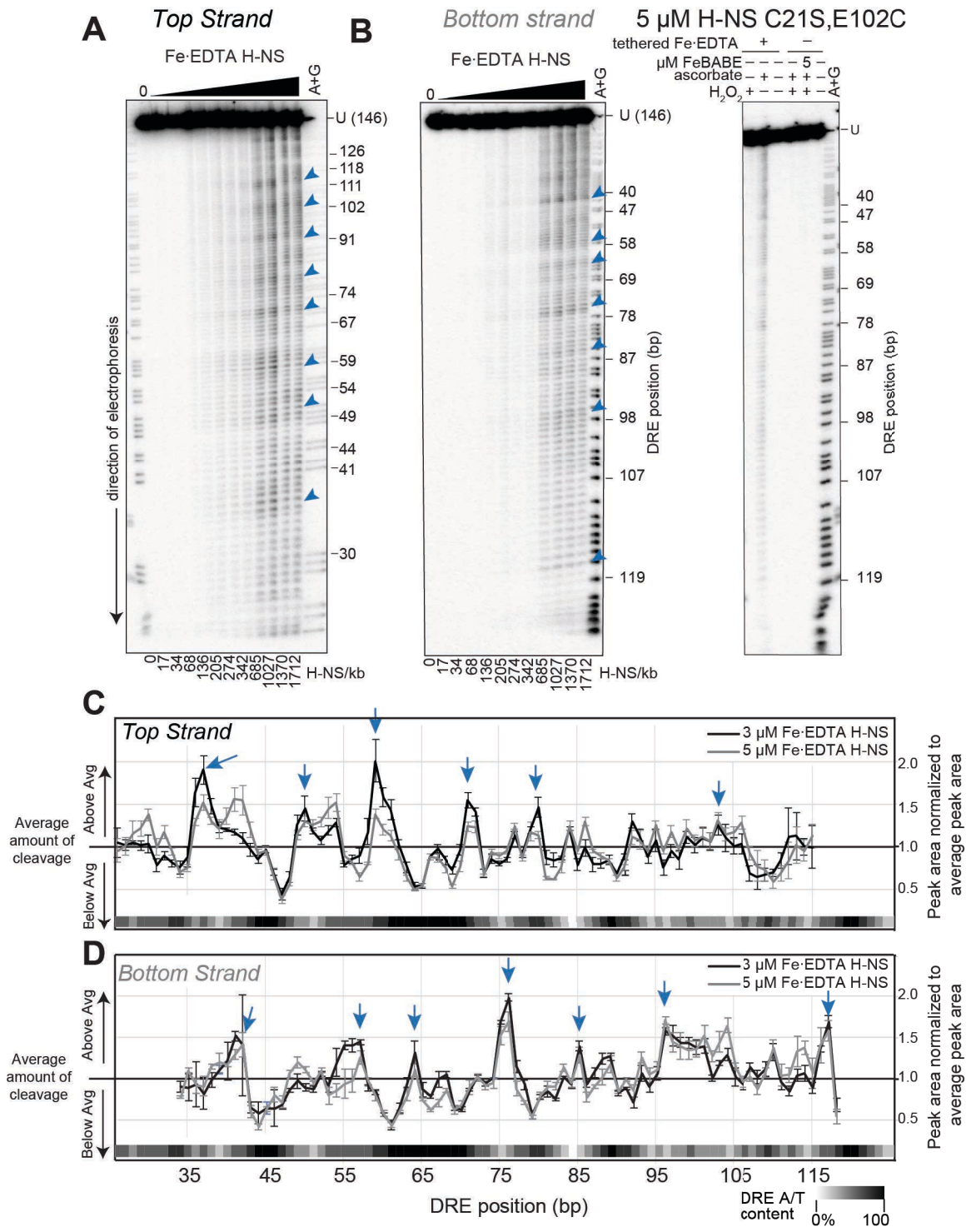

Figure 2. TEN-map locates H-NS DBDs at irregularly spaced sites in the *bgl* DRE.
(A) Denaturing 7% polyacrylamide gel showing Fe^{2+}·EDTA–H-NS cleavage pattern of the 146-bp DRE DNA labeled on the top strand. Increasing concentrations of Fe^{2+}·EDTA–H-NS (50 nM to 5 μM or 17-1712 H-NS/kb) were added to ~20 nM DNA to form filaments. Cleavage was initiated with addition of H_2O_2 and ascorbic acid to 2 mM each. Sites of intense cleavage are indicated with blue arrows. A+G, Maxam–Gilbert cleavages after A and G.

(B) (Left) Same as panel A, but for the bottom strand. (Right) Control reactions on bottom strand electrophoresed next to cleaved DNA. Little to no cleavage was observed unless all components of the TEN-map assay were present.

(C&D) Peak areas calculated by densitometric semi-automated footprinting analysis (SAFA (Das et al., 2005)) and normalized to average signal in each lane for the top (C) and bottom (D) strands (see Methods), shown here for the 3 and 5 μM Fe^{2+}·EDTA–H-NS samples. Peak areas above 1 indicate cleavage hot spots (arrows). Error bars show standard deviation of at least three replicates. The AT content of the DRE fragment (5-bp windows) is indicated by the white-black gradient along the X-axis. See Figure S4 for additional TEN-map controls.

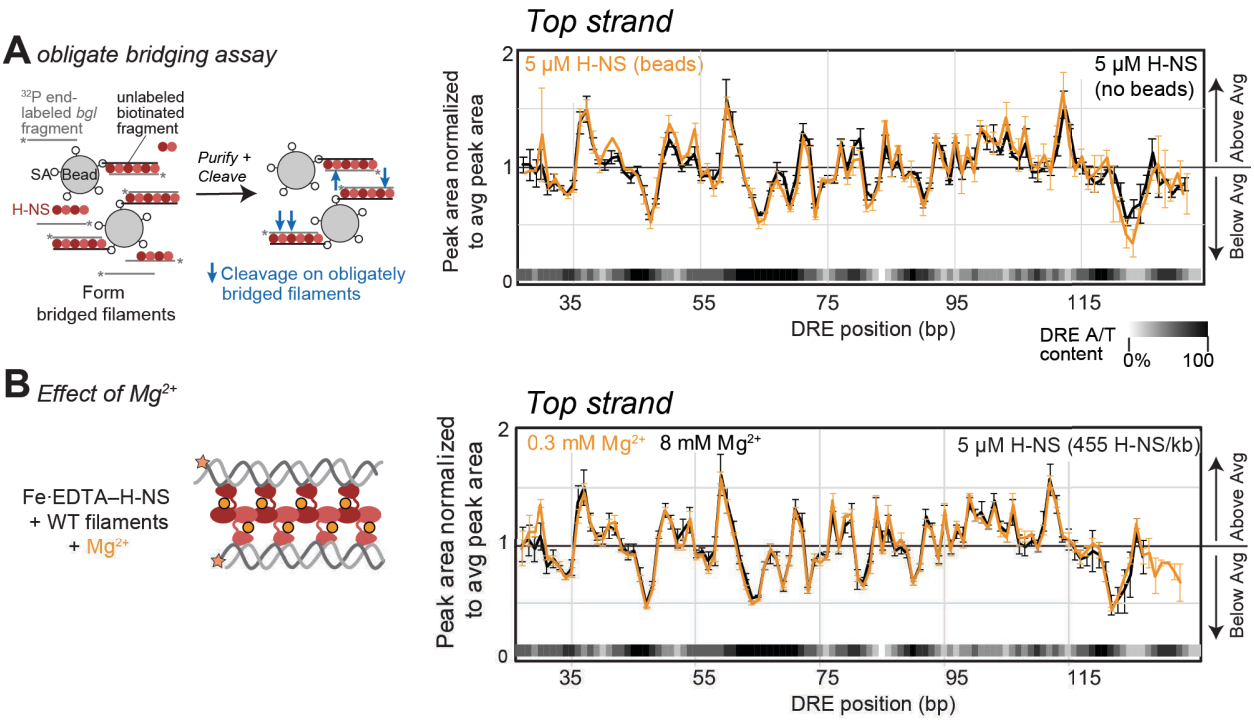

Figure 3. TEN-map reports DBD positions in obligately bridged H-NS filaments.
(A) TEN-map cleavage of DRE DNA is unaffected by obligate bridging. Bridged filaments were formed by mixing unlabeled 685-bp DNA fragment bound to paramagnetic beads, 549-bp DRE-containing DNA labeled on the top strand, and H-NS (60% wild-type H-NS + 40% Fe^{2+}·EDTA–H-NS) at the indicated concentrations. Obligately bridged filaments were recovered by magnetic separation and resuspended in solution containing H_2O_2 to initiate cleavage of DNA (see also Figure S6 and Methods). TEN-map cleavage of the top strand of the DRE region by 5 μM total H-NS (orange) is shown normalized to average peak area in each condition (see Methods). The cleavage pattern is identical to that of the same DNA not tethered to beads (black).

(B) TEN-map cleavage of DRE DNA is unaffected by Mg^{2+} concentration. TEN-map cleavage of DRE top strand by Fe^{2+}·EDTA–H-NS at 5 μM total H-NS (455 H-NS/kb) in the presence of 8 mM (black) or 0.3 mM (orange) Mg^{2+} and analyzed as described for panel A. See also Figures S6-8.

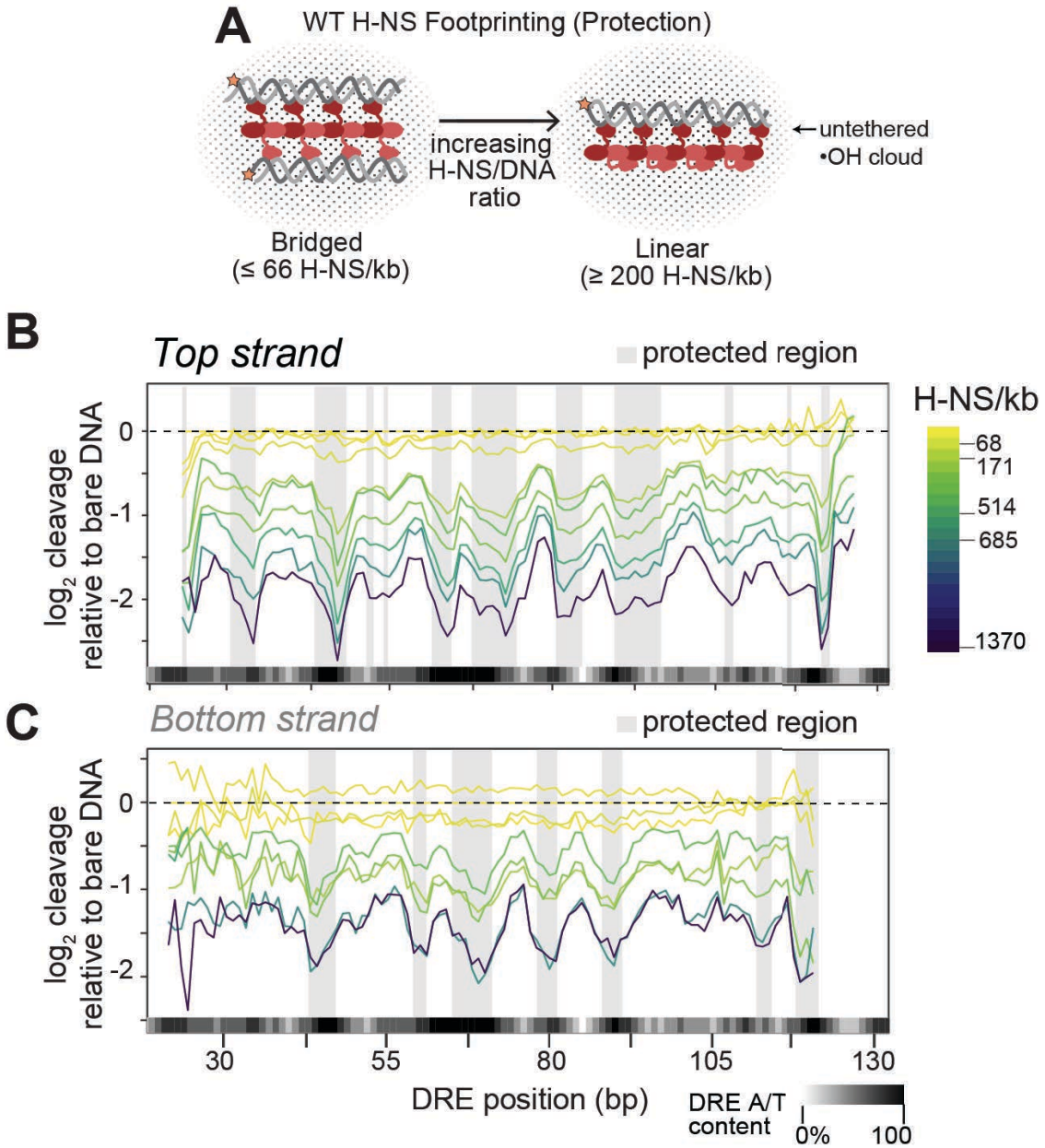

Figure 4. H-NS ·OH footprinting reveals identical protection of the DRE DNA in bridged and linear filaments.

(A) Schematic showing footprinting of bridged and linear H-NS filaments generated by increasing H-NS/DNA ratio using ·OH generated in solution (black dots) (see also Figure 1D). WT H-NS switches from bridged to linear filament conformation when H-NS/kb DNA ≥ ~200 (Kotlajich et al., 2015) (see Figure S2).

(B) Protection patterns on DRE (top strand) at increasing H-NS concentrations (17, 34, 68, 171, 251, 342, 514, 685, 1370 H-NS/kb DNA) are plotted as $\log_2$ ratios relative to intrinsic cleavage of unbound DNA. Strongly-protected regions are highlighted by shaded boxes (see also Figures S9 and S11).

(C) Same as B, but for the bottom strand. In (B&C), lines represent the median of 4 experiments, but error bars are removed for clarity.

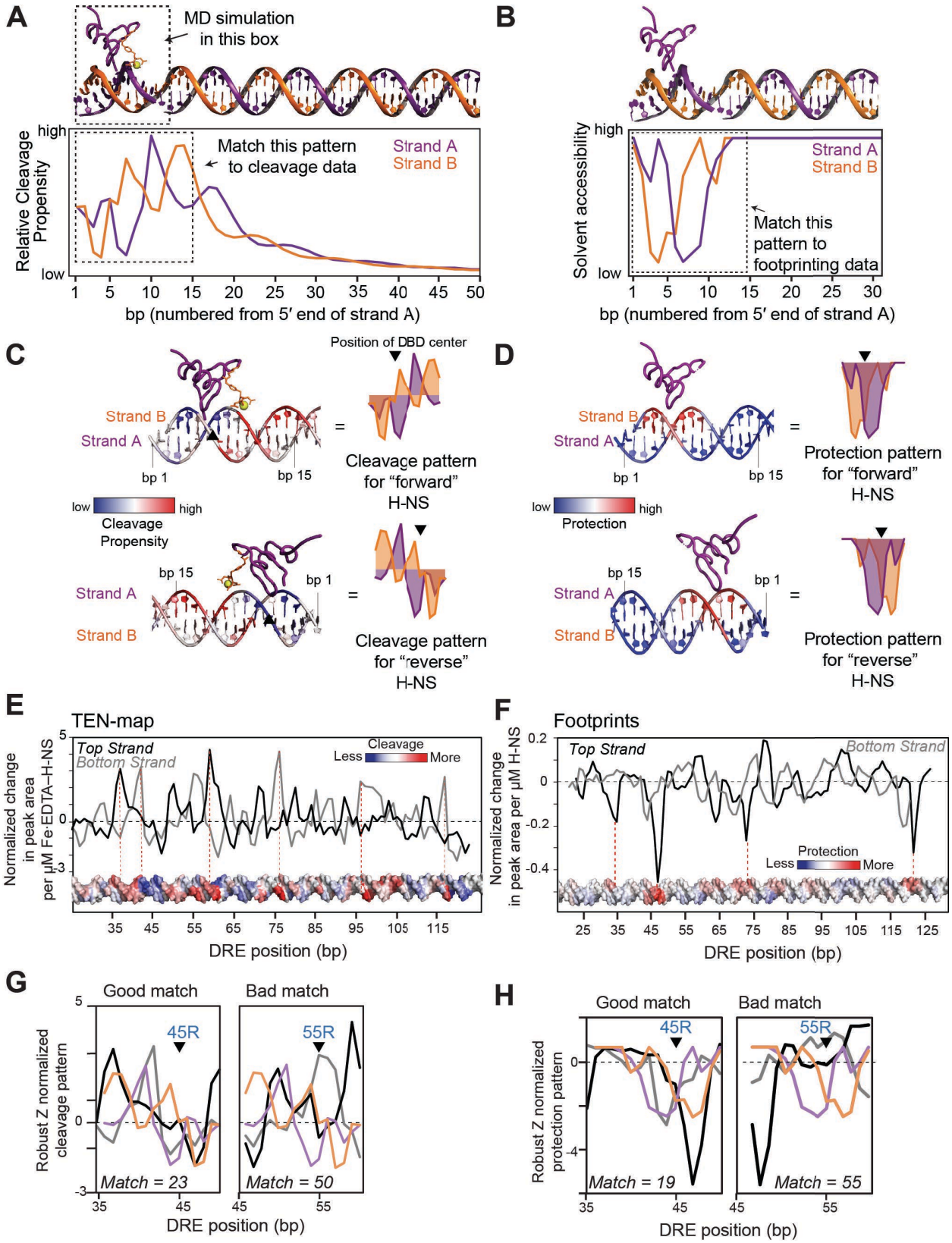

Figure 5. Comparison of predictions from molecular modeling to TEN-map and ·OH footprinting data to place H-NS DBDs on the DRE DNA.

(A) MD simulation of Fe^{2+}·EDTA (orange) conjugated to the H-NS DBD (purple) bound to a 12-bp DNA duplex (strand A, purple; strand B, orange). The distance between the Fe^{2+} and each

bp during the simulation was used to estimate the relative cleavage propensity at each position. Additional DNA (bp 13-50) was included after the MD simulations to estimate cleavage propensities at bp further from the binding site. The cleavage propensity pattern in the dashed box was used in the comparison to experimental TEN-map data.

(B) Solvent accessibility of DNA bound by one H-NS DBD calculated from the structure shown at the top of the panel. A 15-bp portion (dashed box) of this pattern was compared to the experimentally determined ·OH footprinting pattern.

(C) Overlay of the TEN-map cleavage propensity on B-form DNA with H-NS bound in a forward orientation (PDB 2L93) (Gordon et al., 2011). Cleavage propensity is on a blue-white-red spectrum where blue is low cleavage propensity and red is high cleavage propensity. Cleavage pattern of H-NS bound in the reverse orientation is shown below. The black triangle indicates the center of the H-NS binding site used to align predictions and the cleavage data (see panel G).

(D) same as panel C, but displaying the predicted solvent accessibility, or protection, of B-form DNA bound by a single H-NS DBD. Bases more or less protected by H-NS are shown in red or blue, respectively. Slight asymmetry in the protection pattern distinguishes the forward (top) or reverse (bottom) binding directions.

(E) Change in TEN-map signal as a function of H-NS concentration (see Methods and Figure S10). More positive slope corresponds to greater H-NS-dependent cleavage. Error in the calculated slopes is in Figure S10. The slope changes are displayed on B-form DNA with red and blue corresponding to greater or lesser extents of cleavage.

(F) Change in ·OH footprint signal as a function of H-NS concentration (see Methods and Figure S11). More negative slope corresponds to greater H-NS-dependent protection. The slope changes are displayed on B-form DNA with red and blue corresponding to greater or lesser protection.

(G) Examples of alignment of the predicted reverse TEN-map cleavage pattern (panel C) with the TEN-map slope values (panel E) at positions 45 (good match score, 23) or 55 (poor match score, 50). Predicted strand-A cleavage (orange) should match the top strand cleavage pattern (black); predicted strand-B cleavage (purple) should match the bottom strand cleavage pattern (gray). Match scores for the entire DRE fragment are shown in Figure S12.

(H) Same as for G but showing alignment of the predicted protection pattern (panel D) with ·OH footprint slopes (panel F).

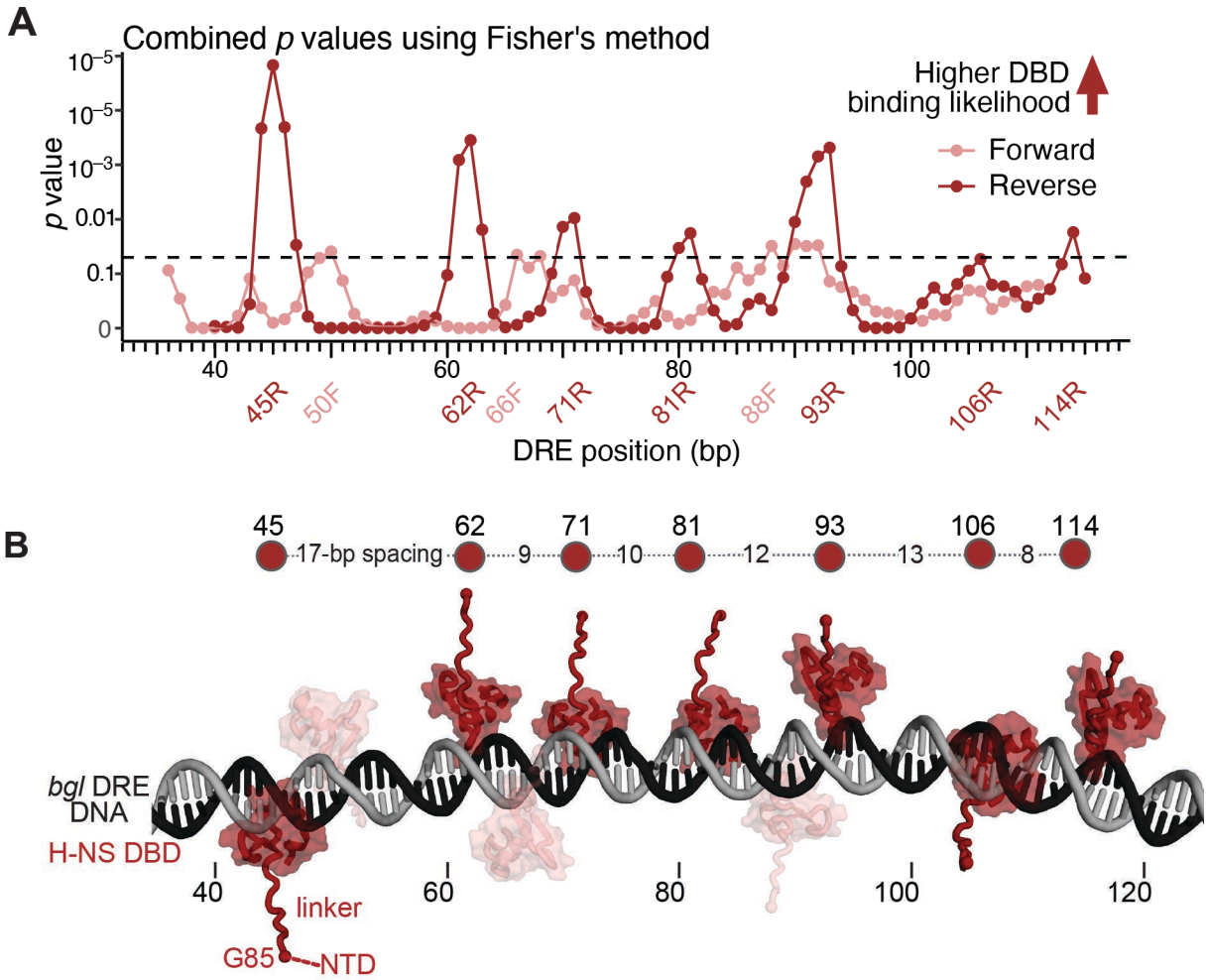

Figure 6. Agreement of MD simulations with TEN-map and footprinting data reveals irregularly spaced binding of H-NS DBDs to the *bgl* DRE.
(A) Evidence for the localization and orientation of the H-NS DBD domain on the DRE DNA by combining evidence for congruency between the MD simulations and the TEN-map data with evidence for congruency between the MD simulations and the footprinting data (see Figure S12; dashed line, p=0.05 Fisher's combined probability test). Evidence is shown as a combined p-value at each base pair in the DRE DNA in the forward (light red) or reverse (dark red) orientations (see Methods for details).

(B) Molecular model of H-NS DBD locations in an H-NS bridged or linear filament on the *bgl* DRE. The DNA model was generated using Nucgen-plus (Bansal et al., 1995). H-NS DBDs were centered at the positions of greatest probability (panel A) in forward (light red) or reverse (dark red) orientations. The reverse orientations are most probable (see text). H-NS DBD model is from (2L93; (Gordon et al., 2011)) and the flexible linker was modeled using AlphaFold2 (Jumper et al., 2021). The spacing between DBDs in the reverse orientation is indicated on the line above the model. The H-NS NTD is not included in the model but would be attached to the DBDs via the flexible linkers.

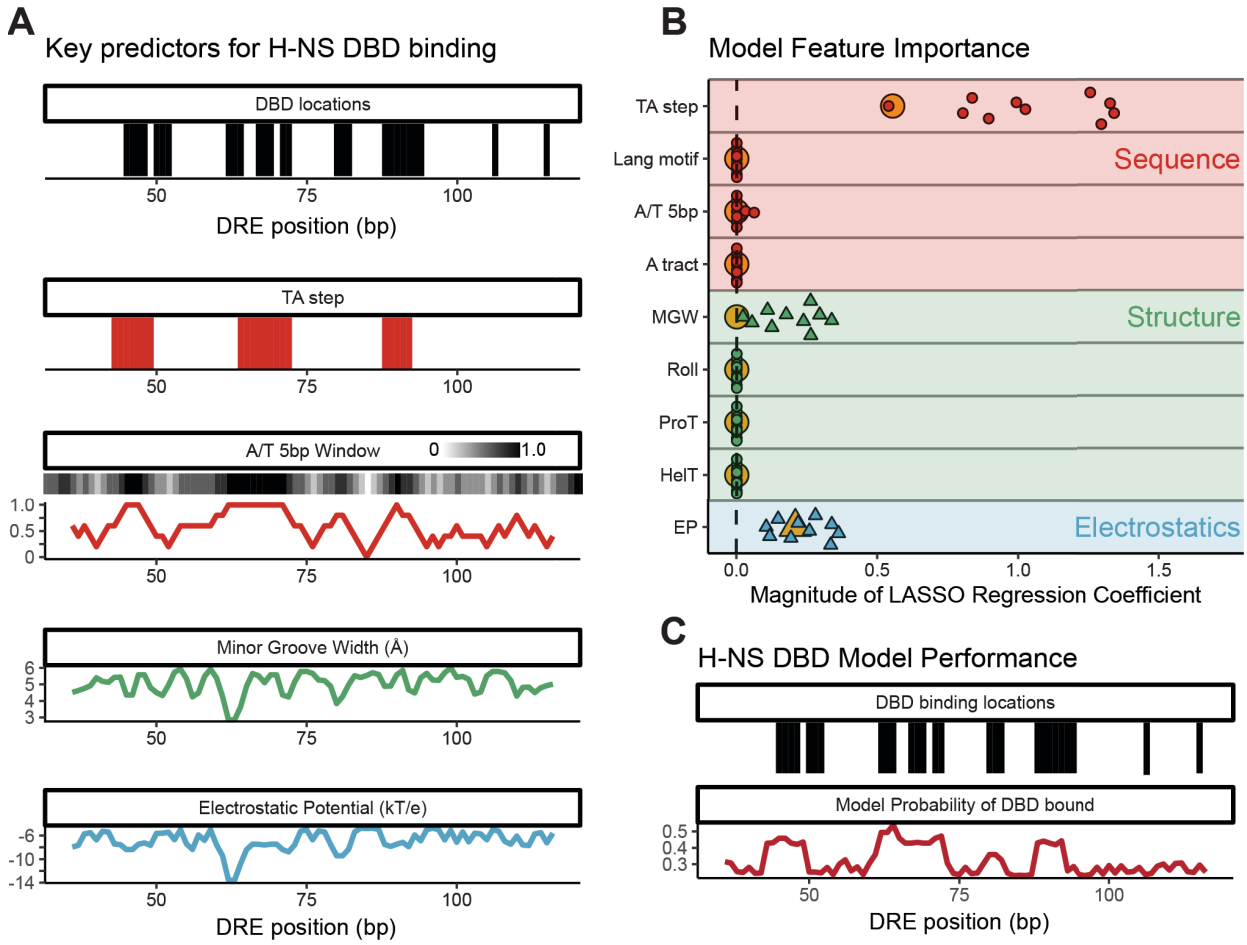

Figure 7. TA steps, minor groove width, and electrostatic potential best predict DBD locations
(A) Relationship between possible H-NS DBD binding locations and the sequence, structural, and electrostatic features of *bgl* DRE DNA. Base pairs with high agreement between the TEN-map and predicted patterns for footprinting and MD simulation in either DBD orientation are represented as black bars ($p \leq 0.05$; Monte Carlo permutation test; see Methods and Figures 5C,D and S12; position 106 is included as nearly indistinguishable from p=0.05). TA-steps are represented as a red bar for every bp within a TA-step 4mer. A/T content averaged over a 5 bp window is shown as a white–black gradient and plot (red) above plots of minor groove width (green) and electrostatic potential (blue) calculated using DNAshapeR (Chiu et al., 2016).

(B) Relative importance of sequence, structure, and electrostatic features in predicting H-NS DBD binding locations. The (+) or (–) valued regression coefficients from a LASSO logistic regression model fitted to the DBD binding locations (Friedman et al., 2010a) are represented as circles or triangles, respectively. Points correspond to coefficients from ten models fit independently by partitioning the data into ten subsets using stratified sampling and fitting each model to a unique set of nine subsets. Large orange symbols indicate the coefficients for a model fit to the entire dataset.

(C) Predictive performance of sequence and structure-based regression model using TA step, minor groove width, and electrostatic potential parameters (panel B). H-NS DBD binding locations (same as in panel A) are shown in black. The probability of DBD binding based on a LASSO regression model fit to the full data set is shown in dark red.

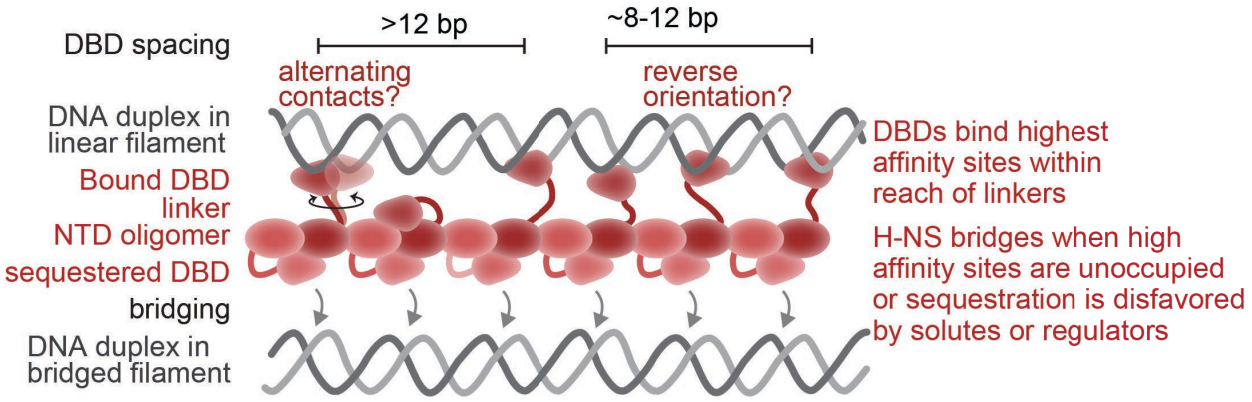

Figure 8. Hemi-sequestration model of H-NS DBD interactions with DNA in bridged and linear nucleoprotein filaments.
In conditions favoring linear filaments, one set of DBDs is sequestered via interaction with the NTD (Shahul Hameed et al., 2018; van der Valk et al., 2017). In conditions that favor bridging, which in vivo could include altered solute composition (Qin et al., 2020), interactions of H-NS modifiers like Hha (Boudreau et al., 2018; van der Valk et al., 2017), or changes in H-NS levels (Kotlajich et al., 2015), the hemi-sequestered DBDs preferentially associate with the same set of irregularly spaced sites used in linear filaments. Variable spacing between DBDs and possible changes in DBD orientation are accommodated within the H-NS nucleoprotein filament by the flexible linkers between the DBDs and the NTD oligomer.